Wind Energy Science

Authors' response to the review comments

Paper title	Fatigue-constrained gradient-based design optimization of main bearing–shaft systems for floating wind turbine drivetrains
Manuscript number	wes-2026-105
Authors	Vasudev Gupta and Amir R. Nejad

(Authors) We would like to express our sincere appreciation to the reviewers for their thoughtful feedback and constructive suggestions and to the editor for expertly managing the review process. We are confident that these comments have helped us to improve the quality of the paper significantly. In response to your feedback, we have made several revisions to the original manuscript. In this document, we aim to address all points raised by the reviewers. All replies to the reviewers' comments are shown in green font. An additional LaTeX diff document has been attached to our response, highlighting all the changes made to the paper.

Referee 1

This paper achieves a multidisciplinary constrained mass optimization method for floating wind turbine drivetrains by introducing Damage Equivalent Loads (DEL) into a gradient-based optimization framework and proposing a main bearing analytical model that accounts for moment-reacting characteristics.

Few comments are listed below:

1. The introduction repeatedly emphasizes the limitations of sequential optimization methods in industry and calls for fully coupled, system-level optimization. However, the experimental setup uses a traditional "two-step global-local decoupled approach," assuming fixed hub loads throughout the drivetrain optimization process. When system mass undergoes drastic changes of up to 48%, the structural frequencies will inevitably shift, subsequently altering the aeroelastic loads. Assuming constant loads weakens the credibility of the "coupled MDAO" core contribution.

- Thank you for your comment, and outlining the inconsistency between the introduction emphasising 'fully coupled, system-level optimization', while the core of the paper discusses the de-coupled optimization of a sub-system of the drivetrain, namely the main-bearing shaft assembly (MBSA), its importance, numerical modelling (structure and fatigue), enhancement of state-of-art drivetrain MDAO toolsets (WISDEM-WEIS) and its efficient design optimization in a gradient-based context. The scope has therefore been clarified, removing the introduction and parts mentioning 'fully coupled, system-level optimization', while detailing MBSA modelling further.

- Certainly, your comment on optimization changing the system geometry and hence changing the turbine structural frequencies is valuable and insightful. As the authors are aware of this and this goes beyond the scope of the paper, the said 'system coupling' is added as a limitation of the work in the conclusion section (Sec. 5.1), with efforts underway to tackle it in detail.

- As a rough estimate, in terms of turbine structure frequencies and its contribution from the drivetrain, the paper focuses on a sub-assembly of the complete drivetrain (the MBSA). However, when the entire drivetrain is design optimized for the given site's load conditions, we observe multiple other constraints as design drivers (like bedplate stress, main bearing deflection etc.) and the overall drivetrain mass (ca. 612 tons) is seen to be roughly the same as the reference IEA 15mw (ca. 630 tons). Hence, with all other components unchanged (rotor and support structure), the drivetrain's contribution to the turbine's structure frequencies would roughly remain unchanged.

2. The optimization process relies entirely on the analytical DEL surrogate model. After obtaining the optimal design (e.g., the converged design in Tab. 9), the paper fails to feed this design back into OpenFAST for full-time-series IEC DLC simulations. This step is crucial to verify whether the bearing fatigue life optimized using smooth DEL still strictly meets the standards in true transient time-domain conditions.

- (Amir) Thank you for your comment. In OpenFAST, the bearings and gears are not modelled in detail. The whole drivetrain is modelled by a simple one-degree of freedom spring-mass-damper model.

- (Vasudev) Thank you. We have taken consideration of your suggestions and the new design (Tab.9, accompanied by a complete drivetrain/nacelle system optimization) is fed back into the high-fidelity wind turbine software SIMA for full time-series IEC DLC simulation runs. Due to the high computational costs, these runs are currently undergoing since days, and we expect to obtain the updated results soon. Although the scope of the paper has been clarified and design feedback loop is beyond the intended scope, the authors are able to give insights into the dynamics with the new revised (complete drivetrain) design only after the deadline (27. Aug. 2026).

3. The authors criticize current research for "utilizing expensive genetic algorithms for drivetrain component design" in the background section. However, in the results section, they only compare the convergence of different gradient calculation methods. There is no direct quantitative comparison of computational time or global optimal solution quality against the criticized gradient-free/heuristic algorithms (like GAs, PSO), leaving the argument for its computational superiority insufficiently supported

- (Vasudev) the reason for criticizing the use of expensive genetic algorithms, or gradient-free optimization (GFO) methods, in general is the following:

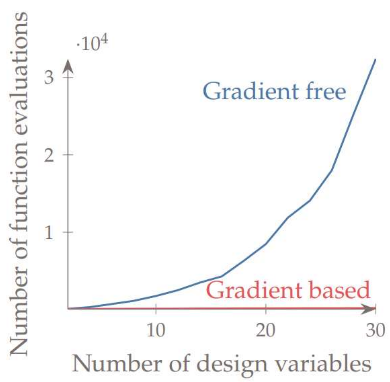

Fig. 1.23 Gradient-based algorithms scale much better with the number of design variables. In this example, the gradient-based curve (with exact derivatives) grows from 67 to 206 function calls, but it is overwhelmed by the gradient-free curve, which grows from 103 function calls to over 32,000.

- (Martins, J. R. R. A. and Ning, A.: Engineering Design Optimization, Cambridge University Press, Cambridge, UK, ISBN 9781108833417,605, https://doi.org/10.1017/9781108980647, 2022.) make clear in their Introduction the limitations of using GFO methods, particularly their computational costs with increasing design variables and more lenient optimality criteria compared to gradient-based optimization (GBO). GFO is thought to be advantageous when, eg. 1. design space is noisy or discontinuous, 2. design variables are discrete (as found in gear-design), 3. derivative cannot be computed and 4. multi-modal design landscape. However, it must be mentioned that GFO don't automatically solve multi-modal problems better than GBO, but GBO with multiple starts (eg. basin hopping) could be more effective and efficient in finding the global optimum.

- The type of optimizer to use majorly depends on the problem being solved. For our model problem discussed in the paper, the design variables are continuous, derivatives are efficiently computed (the paper proposes suitable methodology for areas of drivetrain design where this could be challenging (eg. Bearing analytical gradients, LRD bin-counting) and showcases differences in results section) and multiple initial conditions are shown to converge to the same optima on the design landscape suggesting a global optimum.

- Taking consideration of the reviewer's comments, the NSGA-2 GFO algorithm (commonly used in literature for gearbox optimization) was applied to our model problem but the optimizer is seen to fail and not converge within the termination criteria (of 300 generations).

- From our use of GFO method in drivetrain design, particularly medium-speed gearbox (GB) optimization with approximately 30 design variables, the computational time was nearly on the order of one-day, such costs being unsuitable for drivetrain-system optimization, let alone coupled with other turbine components. A recent GB study from our Made4Wind project (https://doi.org/10.5194/wes-2026-90) proposes a hybrid optimization strategy (exploiting both gradient-based and -free stages) for GB optimization and shows its computational benefits in terms of costs (times in order of minutes) and multi-objective pareto optimum.

Referee 2

Comments

Technical comments:

1. Although the paper discusses coupled and system-level optimization, the hub loads are kept fixed, and the optimized design is not fed back into OpenFAST to calculate updated loads. The authors should clarify how coupled the presented method actually is.

- (Vasudev) Thank you for your comment. We observe that it is very similar to Referee 1's comment #1 and #2. We therefore refer the reader to those points above where they are addressed to the best of our capabilities.

2. The main bearing configurations chosen for the paper needs more justification/discussion. In terms of both why these specific bearing types are used in

these positions and why a double main bearing configuration is used instead of a single main bearing configuration.

- (Vasudev) Thank you for pointing this out. Indeed, it is an important aspect of the discussion and therefore a new section (Sec. 2.2 'Comparative study on different drivetrain concepts') has been added to further explain the chosen main-bearing rotor-support configuration employed in the study.

3. The rotational stiffness of the bearing is quite important in determining the results obtained. A discussion of how such a value was obtained is missing. Especially important would be its change with respect to differing bearing dimensions.

- (Vasudev) Thank you for your insightful comment. Yes, the rotational stiffness of the bearing is an important parameter, especially for the design equations proposed in the paper. It is estimated using power-law regression on database of known bearing specifications, relating its bore diameter to the tilting stiffness. Therefore, a new section (Appendix Sec. D) about it has been added.

4. Section 2.3.3 onwards: Inconsistency between LRD and LDD: LRD has been discussed but some amount of discussion and a figure is made while discussing LDDs.

- (Vasudev) Thank you for pointing out this typo-error from my side. The discussion was only around LRD and the respective texts that mention it has been corrected.

5. "The model enhances design accuracy and setup validity, matching real drivetrain physics better compared to the low-fidelity analytical equations." This statement is to be further justified.

- (Vasudev) Thank you for your comment. The respective Sec. 2.5 has been updated with further details about the structural solver model to justify the statement.

6. Section 4.1: Results are presented but not discussed.

- (Vasudev) Thank you, more details of and discussion about the results has been added in the section.

Structural comments:

1. Add a list of abbreviations to improve comprehensibility of the paper.

- (Vasudev) Thank you for the suggestion, it has been added in the appendix (Sec. E2)

2. Not all figures, equations and tables in the paper are referred to within the text.

- (Vasudev) Thank you, the manuscript has been revised with relevant changes.

3. When multiple sub-figures are part of a figure, please label each of them individually.

- (Vasudev) Thank you for the suggestion, this has been added to e.g. Fig.15.

4. Overall, derivations and formulas need to be explained in more detail and with each variable described for comprehensibility.

- (Vasudev) Thank you for the clarification. The derivations have been revised for better comprehensibility.

5. Please make the citations consistent. Some appear to, for example, have important details, like the year of publication missing.

- (Vasudev) Thank you for making us aware. The citations were checked and corrected.

Editorial support team

1. Please note that section "Author contributions" should only include initials of the author names. Please see guidelines at: https://www.proceedings-iahs.net/submission.html#manuscriptcomposition
2. Please ensure that the colour schemes used in your maps and charts allow readers with colour vision deficiencies to correctly interpret your findings (see e.g. Fig. 19). Please check your figures using the Coblis Color Blindness Simulator (https://www.color-blindness.com/coblis-color-blindness-simulator/) and revise the colour schemes accordingly.

- (Vasudev) Thank you for your consideration and suggesting fixes. Both have been incorporated in the revised manuscript.

Fatigue-constrained gradient-based design optimization of main bearing–shaft systems for floating wind turbine drivetrains

Vasudev Gupta[1] and Amir R. Nejad[1]

[1]Department of Marine Technology, NTNU, Professor JHL Vogts veg 1a, 7052 Trondheim, Norway

Correspondence: Vasudev Gupta (vasudev.gupta@ntnu.com)

Abstract. Floating offshore wind turbines have significant potential for economical and environmentally-efficient solutions for energy production. However, current state-of-the-art witnesses a lack of integrated analysis and optimization of these large, dynamically-coupled complex engineering machines and their critical sub-systems, such as the drivetrain, with research and experience still in their infancy. The aim of the paper is to facilitate efficient and holistic gradient-based multi-disciplinary constraint optimization of drivetrains by exploiting numerical models with varied fidelity-levels. This is illustrated through a constraint optimization of the main-shaft assembly, which includes critical fatigue-limit constraints of main-bearings, bridging design load case-based load spectra reduction with analytically-differentiable damage equivalent loads in contrast to conventional non-smooth bin-counting. The importance of fatigue as a design driver is shown by comparison to only static structural design. The proposed methodology is implemented as a modular extension within the open-source WISDEM-WEIS framework based on OpenMDAO, enabling efficient integration into existing multidisciplinary system-level wind turbine design workflows.

1 Introduction

1.1 ~~Multidisciplinary optimization of floating wind~~

Wind turbines (WTs) are inherently multi-disciplinary complex engineering systems, that must withstand extreme stochastic environmental conditions (ECs), satisfy relevant mechanical constraints while producing the highest possible energy at the lowest possible cost. Such are a difficult class of problems to solve, challenging the wind energy and design-optimization state-of-the-art (SoA)~~.~~

~~The wind energy community recognises that the current industrial practice of optimizing each component decoupled from the others and sequentially leads to suboptimal design, sometimes being even inconceivable from a system-level perspective (Perez-Moreno et al. (2016); Veers (2019)). Moreover, several research studies (Jasa et al. (2022); ?); Dykes et al.) give evidence to an optimal consequence when disciplines are integrated and optimized simultaneously for a technical-economic-safety objective.~~

~~Therefore, the need to exploit the multidisciplinary nature of WT and to shift to a multidisciplinary design, analysis and optimization (MDAO) basis (Martins and Ning (2022)) contains a huge opportunity for wind energy systems -~~ , and a science that is still in its infancy.

1.1 The need for reliable and optimized drivetrains

The potential of offshore wind cost reduction is high (Musial et al. (2022)), with economics projected to decrease further between 2021-2030. Trends in industrial applications and research literature show that there is not yet a consensus on the optimal drivetrain (DT) design and technology for large multi-MW floating offshore wind turbine (FOWT) applications.

Drivetrains significantly influence the operational reliability and availability of WTs. The unique and harsh operational conditions (OCs) - unsteady loads, high torque variations, axial/thrust loading, parasitic non-torque loads (NTLs), slow rotational speeds (rpm) - that they undergo make their premature failure rates, long downtimes and repair/replacement costs a concern for the wind industry (~~Nejad (2018); Veers (2019); Wenske (2022); Nejad et al. (2022); Dao et al. (2019)~~Nejad (2018); Veers (2019); Wenske).

With regards the critical components of a wind turbine, and amongst them the drivetrain assembly – comprising of the drivetrain (shafts, bearings and brake), gearbox and generator, Dao et al. (2019) reports its contribution to failure rates as roughly 12.5% onshore and 33.3% offshore, while contributions from downtimes and repair times (in hours) being amongst the highest, the former estimated to be roughly 63.6% onshore and 77.7% offshore.

With regard to main bearings (MBs), Hart et al. (2023) recently investigated a large dataset of 7,707 WTs and documented significant signs of premature failure, with the locating (thrust-carrying) bearing being the vast majority, and their life largely deviating from standard-based estimations: 10% failure in 10.5 years. At 20 years design life, predicted failure rate was 22-25%. Literature (Chovan and Fierro (2021); Guo et al. (2015a); Wenske (2022); Link et al. (2011)) reasons that in large (multi-MW) WTs, even under normal OCs, unfavourably high axial-to-radial load ratios (F_{ax}/F_{rad}) cause unequal load sharing between roller rows of flexible MB setups. Consequently, NTLs and axial displacements enter the gearbox (GB), causing unequal load sharing between planet bearings and meshing gears, that enter into deteriorating regimes. A recent NLR report shows that, of the most prevalent GB failures on onshore WTs, 76.2% are due to GB bearings (Veers (2019)). The GB is also one of the most expensive and heaviest components of a WT-DT. Overall, these phenomenon reduce the reliability and life of the entire DT (Chovan and Fierro (2021); Wenske (2022)).

The current state-of-the-art review concludes that bearings are critical reliability drivers in wind energy, especially offshore wind, and that addressing fatigue failures are amongst the top technical challenges in lowering costs of energy.

1.2 Drivetrain multi-disciplinary design optimization

Novel DT designs for large WTs involve a complex and collaborative process, meeting several technical requirements simultaneously.

Current SoA WT DT analysis is seen to exploit sequential design loops, treating bearings using static load checks with decoupled L_{10}-life post-processing, and exploiting expensive genetic algorithms for DT component design. In general, design criteria involving structural dynamics and fatigue damage are rarely seen in floating offshore wind turbine (FOWT) optimization, (Patryniak et al. (2022)).

Detailed DT design ~~fully-coupled with~~ within efficient gradient-based optimization (GBO) and inclusion of critical fatigue metrics within the system-scope is yet to be seen in wind energy research and industry, which has significant potential for novel solutions: high energy production at increased reliability and lower costs (~~Wenske (2022); ?); Guo et al. (2017); Hart et al. (2022)~~ Wenske (2022); Sethuraman et al. (2018); Guo et al. (2017); Hart et al. (2022)).

The present research aims to elucidate on an important topic: ~~**the lack of integration and details of drivetrain design in aero-elastic analyses and system-level FOWT optimization**~~the lack of integration and details of drivetrain design in aero-elastic analyses and system-level optimization.

1.3 Numerical frameworks

To enable drivetrain MDAO within the system-scope, the present paper exploits `WISDEM`, a comprehensive WT system engineering MDAO framework developed by NLR (2026)[1], which codifies physics-based computational and empirical models for WT component optimization and cost estimation. `WISDEM`'s key benefits lies in its computational efficiency – inexpensive and fast – to perform steady-state system-level techno-economic (LCOE, AEP) MDAO, conduct preliminary sensitivity studies between coupled components, and quickly access performance trade-offs between potentially viable designs.

However, in light of drivetrain analysis, `WISDEM`'s current module (`DrivetrainSE`) lacks detail and is insufficient to optimize critical component, falling behind the current industry's performance capabilities (WISDEM-GitHub (2026)). Moreover, its workflows focuses on sizing and cost, but critical metrics such as fatigue-based reliability and safety margins at the component level (e.g. bearings) are not yet integrated. Given `WISDEM`'s benefits, this creates a gap for the wind energy research and development industry.

1.4 Objective and novelty of the work

The purpose of this study is to fill this gap by introducing detailed bottom-up physics-based drivetrain optimisation within `WISDEM-DrivetrainSE` through

1. targeting high impact and critical drivetrain components (e.g. MBs) through coupling between geometry design variables and fatigue safety factors directly in optimization to significantly improve drivetrain design robustness,

2. bridging of design load case (DLC)-based operating-load variable-speed spectra reduction with analytical damage equivalent load (DEL) for bearing fatigue,

3. integration within an efficient GBO framework,

[1]National Laboratory of the Rockies; formerly the National Renewable Energy Laboratory (NREL)

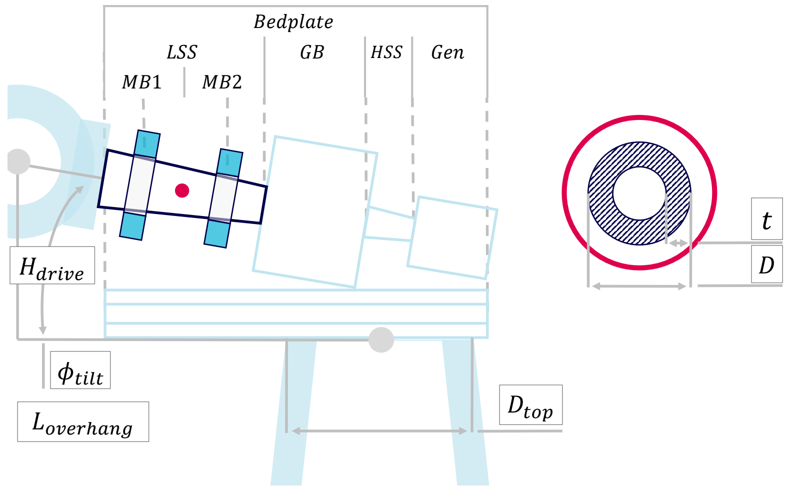

Figure 1. Geared Drivetrain Layout for the Made4Wind 15MW

4. scalable and industry-relevant gradient-consistent drivetrain multi-disciplinary optimization (and integration into MDAO workflow, eg. the `openMDAO` framework).

Such would ~~enable~~ facilitate further research on:

1. drivetrain optimization as a component within the wider WT system-scope~~.~~,
2. coupled dynamics between turbine components, especially interactions of floating substructure (platform motions), sea states, drivetrain (loads) and control strategy on large FOWTs~~.~~,

~~ultimately enhance~~ enhance confidence in the resulting optimal design and ultimately insights into system-level interactions.

The use case scenario is the IEA-15MW floating reference WT supported on Acciona's CT-bos tension leg platform (TLP) (Sect.A).

1.4.1 Scope of the work

The paper presents a practical design optimization methodology for the drivetrain components that are first in line in the load path from the aerodynamic rotor blades, namely the ~~main-shaft assembly (MSA~~main-bearing shaft assembly (MBSA; Fig.1), comprising the main shaft (conical, hollow and of steel material (Tab.B2)) and the two main bearings, which support the former, the rotor assembly (hub and rotor blades) and the first-stage GB carrier, Fig. 2.

~~Due to high reliability requirements for large-FOWT DTs, as well as observations from recent field tests, there is a shift in focus from flexible to rigid DT configurations utilizing preloaded moment-reacting tapered roller bearings (TRBs) with high contact angles as MBs and first stage planet carrier bearings (Chovan and Fierro (2021); Guo et al. (2015a); Wenske (2022); Link et al. (20). Therefore, the selected MB configuration is MB1 being floating, reacting to radial loads (e.g. CRB), while MB2 being~~

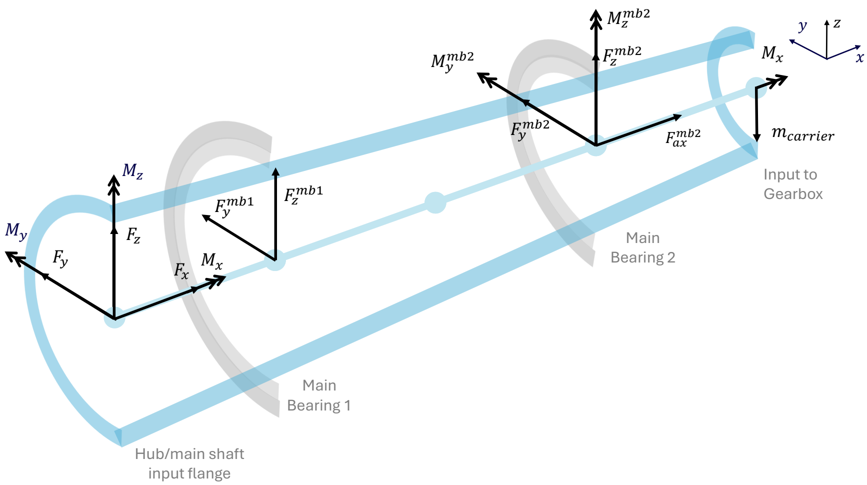

Figure 2. ~~Main-shaft~~ Main-bearing shaft assembly (~~MSA~~MBSA) with respective component loads

~~fixed/locating, reacting to axial, radial and part of bending (tilting) moment loads (e.g. double-row TRB or TRB2). Such moment-reacting (MR) bearings provide angular stiffness and can transmit bending moments through the rolling-element contact.~~

2 Methodology

2.1 Initial design and load cases (DLCs)

This work employs the conventional de-coupled (or 2-step) global-local approach~~for drivetrain analysis assuming~~ , which assumes fixed hub loads throughout.

To initiate the turbine's design optimization process, some representative (hub) loads are required. The loads acting on the turbine (and its structural components) dictate its sizing which must satisfy the relevant limit stress utilizations and fatigue constraints.

To this end, an initial global FOWT model – representative of the Made4Wind 15MW with a medium-speed 3-stage planetary geared drivetrain, standard floating tower (Allen et al. (2020)) and Acciona's CT-bos TLP substructure – was created in the aero-hydro-servo-elastic simulation software ~~openFAST~~SIMA to facilitate IEC DLC simulation and loads extraction.

The respective aerodynamic hub load channels extracted from ~~openFAST~~SIMA outputs are listed in Tab.1. The coordinate system is centred at the main shaft-hub interface, non-rotating, and aligned with the tilted low-speed shaft (LSS) (as in A.3, DNV (2016)).

2.1.1 ULS: Steady-state extreme loads

Ultimate limit state (ULS) criterion defines a design based on the ability to withstand long-term extreme-occurring loads for a given lifetime, which can be estimated using either of the following 2 methods:

1. Probabilistic extrapolation of loads from DLC with normal operating condition.
2. Maximum occurring loads of DLCs with extreme operating conditions.

The second method, similar to the IEA 15MW turbine reports (Gaertner et al. (2020); Allen et al. (2020)), is used in this study and is described as follows:

A selected subset of IEC DLCs – defining normal and extreme environmental conditions, start-up, shutdown, emergency stop and ~~yaw-misaligment~~ yaw-misalignment – were analysed, wherein the maximum rotor-hub loads were extracted and compared across the DLCs. It was observed that DLC ~~5.1 (Emergency stop~~4.2 (Shutdown during extreme operating gust) resulted in the largest overall rotor-main shaft ~~torque~~ forces and bending moments, which are design drivers for the sizing of drivetrain components, eg. the GB and ~~MSA respectively. Moreover, DLC 3.2 (Extreme gust) resulted in the highest~~ MBSA respectively, with axial/thrust loads ~~, which are~~ particularly critical for the design and operation of MBs or ~~MSA~~MBSA. Therefore, these maxima values were selected and are presented in Tab.2.

Table 1. Main shaft hub loads extracted from respective ~~openFAST~~ SIMA channels, at 20Hz sampling frequency (or step size $\Delta t = 0.05$s).

Notation	Load	Channel	~~Shape~~Array shape
$\mathbf{F}_x$	Thrust	~~RotThrust~~ShaftFx_[N]	~~array~~[~~7200~~36000,10]
$\mathbf{F}_y$	Shear	~~LSShftFys~~ShaftFy_[N]	~~array~~[~~7200~~36000,10]
$\mathbf{F}_z$	Shear	~~LSShftFzs~~ShaftFz_[N]	~~array~~[~~7200~~36000,10]
$\mathbf{M}_x$	Torque	~~LSShftTq~~ShaftMx_[N-m]	~~array~~[~~7200~~36000,10]
$\mathbf{M}_y$	Pitching	~~LSSTipMys~~ShaftMy_[N-m]	~~array~~[~~7200~~36000,10]
$\mathbf{M}_z$	Yawing	~~LSSTipMzs~~ShaftMz_[N-m]	~~array~~[~~7200~~36000,10]

Table 2. ULS hub loads for drivetrain design optimization

~~Load~~load	x	y	z	units
F_*^{max}	~~5.39~~ 8.0	~~1.36~~ 10.8	~~5.57~~ 11.0	~~MN~~ [MN]
M_*^{max}	~~52.51~~ 21.5	~~107.46~~ 76.5	~~99.48~~ 35.8	~~MNm~~ [MNm]

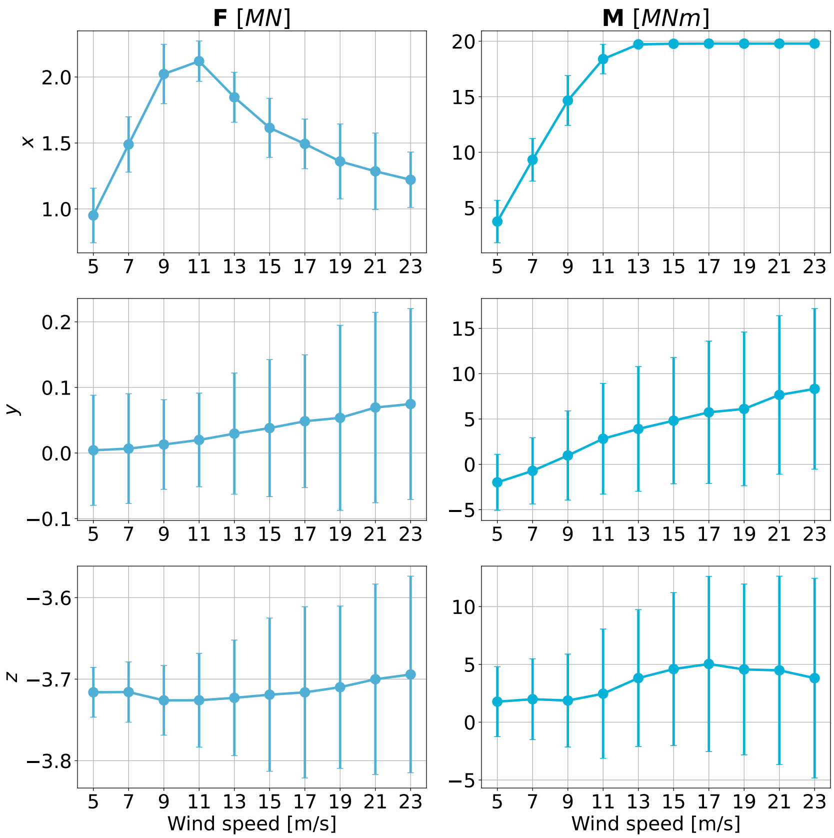

Figure 3. Mean and standard deviation of hub/main-shaft loads;
$\mathbf{F}$-forces and $\mathbf{M}$-moments, in x, y, z-directions.

2.1.2 FLS: Transient full DLC load matrix

Fatigue limit state (FLS) criterion defines a design based on the ability to withstand fatigue loads (cyclic or repeated loading) during the design lifetime of the component.

From aero-elastic simulations of DLC 1.2, the 6-DOF hub forces and moments time series, respectively, acting on the hub flange-main shaft interface were extracted; denoted $\mathbf{F}_*$ and $\mathbf{M}_*$, Tab.1 and Fig.3.

These raw hub loads time series are piped directly into the new analytical main bearing component within `DrivetrainSE` to formulate fatigue life constraints, as described in the Sect.2.3.

In the following, index j defines the wind speed bin (eg. $[1, 2, ..., 10]$), while i defines the time step instance (eg. ~~$[1, 2, ..., 72000]$~~ $[1, 2, ..., 36$

2.2 Comparative study of different drivetrain concepts

Before diving into the different available DT concepts and their respective characteristics, a comprehensive understanding of the loads acting on the DT must precede.

Due to rotor weight overhang and externally-induced loads (aero, hydro, and electro), the DT is subjected to pure-torque and non-torque loads (NTLs), which include translation forces (F) in all 3 directions, pitching and yawing bending moments.

NTLs, being termed ‘parasitic loads’, are often underestimated and their load effects have gained insufficient attention (Wenske (2022)). If not addressed properly and holistically, they adversely affect the reliability and life of DT components.

MBs: Unfavourably high axial-to-radial load ratios (F_a/F_r) in large-MW WTs under normal OCs have caused unequal load sharing between MB roller rows, has lead to premature fatigue damage and failure of MBs much earlier than the design lifetime, and to the entrance of loads and axial displacement into the GB, that ultimately reduce the reliability and life of the entire DT (Chovan and Fierro (2021); Wenske (2022)).

GB: In real-world turbine operation NTLs, through the main shaft (MS), contribute significantly to GB problems (Link et al. (2011); Guo) - minute displacements or NTL bending moments cause unequal load sharing of:

1. ring-planet gear meshing: entering into deteriorating regimes of reversing tooth-edge contact leading to high localized stress and hence gear tooth damage.

2. planet bearings: leading to periodic out-of-phase bearing row loads, with the upwind side majorly loaded, inducing motions and deformation misalignment into the GB.

3. planets: represented by the planet load sharing factor which increases with NTLs’ magnitude, and could be well beyond ’disturbed load sharing’ regime, entering into ’tooth edge contact’ regime or even worse ’reversing contact loading’ regime (undergoing up- and down-wind periodic contact), significantly reducing GB life.

2.2.1 Main-bearings type selection

In flexible MB setups (e.g. with SRBs), the unfavourably high drivetrain loads in large-MW WTs have caused unequal load sharing between roller rows in MBs (observed in both 3- and 4-pt. suspension systems, although the latter system’s damage takes longer to develop), such that the downwind row is heavily loaded and sometimes taking the entire thrust load. Flexible setup’s low rigidity with necessary internal clearance leads to premature fatigue damage (wear, spalling, micropitting etc.) and failure of MBs much earlier than the design lifetime. Because maximum axial shift (main shaft displacement) depends on the said internal clearance, loads and axial displacement consequently enter the GB, reducing the reliability and life of the entire DT.

Field experience from operating WTs shows that TRBs (due to preload) have higher reliability than SRBs, especially for large ($>$ 8MW) FOWTs (Wenske (2022), pg.514 pdf & Guo et al. (2015a)).

The above point is further emphasised in a study by Timken (Chovan and Fierro (2021)), comparing SRBs and TRBs as main shaft bearings for large FOWTs and concluding that high reliability requirements for WT DTs has shifted the focus to using preloaded TRBs.

1. Observing roller-raceway condition after a given years of operation, the unequal load sharing in SRB-MBs shows early signs of micropitting damage development. These signs of metal-to-metal contact were observed to be absent from the preloaded TRB-MBs via visual inspection and pulse shock monitoring (a condition monitoring (CM) technique for mechanical systems that rotate slowly).

2. Effects of NTLs are depicted by quantifying axial displacement in the main-shaft (MS) assembly and its connection to the GB. Operational tests show displacements of TRB-MBs being significantly lower than those of SRBs, by as much as a factor of one-third (1/3). This is due to the internal clearance of SRBs as opposed to the favourable preloading in TRBs. Moreover, higher contact angles are also shown to directly result in lower axial displacements.

(Wenske (2022)) comments on the influence of rotor size / MW-rating of the wind turbine on MB selection and states that, "for modern large WTs, TRBs are now the preferred MB solution, with manufacturing capabilities sufficient to provide TRBs for large ($\geq$ 20 MW) WTs".

Due to high reliability requirements for large-FOWT DTs, as well as observations from recent field tests, there is a shift in focus from flexible to rigid DT configurations utilizing preloaded moment-reacting tapered roller bearings (TRBs) with high contact angles as MBs and first stage planet carrier bearings (Chovan and Fierro (2021); Guo et al. (2015a); Wenske (2022); Link et al. (20).

2.2.2 Rotor-support configuration selection

Research as well as commercialized WTs have utilised different configuration setups to support the rotor via the MBs, among them being double MB (DMB), single MB (SMB), common housing-bearing unit, Alstom PureTorque and a single large moment bearing; each characterising different DT compactness, load paths and degree of mechanical integration (i.e. multi-purpose design elements).

Prior to the process of DT optimization, a brief comparison of the first two DT setups (DMB and SMB) is provided, based on documented industrial experience, DT design strategies in terms of load path and configurations' influence on WT reliability and O&M. A holistic comparison with other support setups mentioned is planned as future work.

The 3-point or SMB configuration due to its comparatively simple design, compact and lightweight nacelle and cost effectiveness, could be a favourable setup to support the hub and drivetrain. However, field experience shows that disadvantages seen for this support configuration offset the advantages, especially with high reliability requirements for multi-MW WT DTs.

1. High MB wear and field failures reported during operation, which adversely affects gear meshes and loads inside the GB.

2. For 1-3 MW WTs, higher (nearly double) fatigue failure (22-30 %) and replacement rates in 20-year lifetime than DMB systems (15 %), as well as higher GB average annual failure rate (5.9 %) – compared to 0.8 % for the latter (Nejad (2018); Hart et al. (2020)).

3. GB becomes a load carrying structural member (i.e. it should absorb or react to NTLs), possibly inducing deformations into first gear stage, which reduces GB reliability (Wenske (2022); Link et al. (2011)).

Moreover, 4-point or DMB are seen to:

1. Minimizes the introduction of NTLs into the GB and isolates GB vibrations, as these loads are transferred to the second bearing and the main frame (Helsen et al. (2012); Torsvik et al. (2018)).

2. Have high level of stiffness for all NTLs, comparatively simple GB replacement, good serviceability due to separate structures and functionality (low-integration) (Wenske (2022))

However, these come at the cost of increased weight, space constraints, CapEx costs, as well as sensitivity to assembly tolerances and frame deflection (bearing play).

Floating-fixed bearing layout:

Observations from common industrial practice and engineering insights on drivetrain layout suggest that the upstream bearing (MB1) should be floating (axially-free) while the downstream bearing (MB2) should be locating (axially-fixed). This is to better distribute the bearing forces, regulate their reactions and hence their size constraints. MB1 experiences very large radial loads and therefore it is better to let MB2 take up axial/thrust loads, in addition to radial (and possibly moment) loads.

2.2.3 The selected main-bearing rotor-support configuration

Therefore, the selected drivetrain configuration for this study is the DMB setup with MB1 being floating, reacting to only the radial loads (e.g. CRB), while MB2 being fixed/locating, reacting to axial, radial and part of bending (tilting) moment loads (e.g. double-row TRB or TRB2). Such moment-reacting (MR) bearings provide tilting/rotational stiffness and can transmit bending moments through the rolling-element contact.

2.3 A Fast and Representative Model for Suspension Setups with Moment-Reacting MB2

In the following, a new numerical methodology is devised that enables fatigue limit state (FLS) bearing constraint in an efficient and modular manner for holistic design optimization and propels MDAO studies on wind turbine drivetrains. Based on the MDAO framework `openMDAO` and supplemented in `DrivetrainSE`, it overcomes the latter's limitation of steady-state extreme-loads (ULS) driven analysis and design for drivetrain configuration and components.

Guo et al. (2017): "This analysis is driven by extreme loads and does not consider fatigue. Thus, the effects of configuration choices on reliability and serviceability are not captured."

Several studies, such as early NLR drivetrains Guo et al. (2015b)), formulate the analytical low-fidelity load equations assuming no moment-reaction on the locating bearing – only valid for non-moment reacting (non-MR) bearings such as SRBs, CRBs etc. – in order to render a statically-determinate model which can be solved using closed-form equations (Eq.1 and 2 for MB1 and MB2 respectively).

With

$$x_3 = (L_{h1} + L_{12})$$
$$g_x = g\ \sin(\phi)$$
$$g_y = 0.0$$
$$g_z = -g\ \cos(\phi)$$

MB1 reactions:

$$\begin{aligned}
&\text{using} \sum \mathbf{M}^{mb2} = \mathbf{0}: \\
&\qquad \mathbf{F}_{ax}^{mb1} = \mathbf{0} \\
&\qquad \mathbf{F}_{y}^{mb1} = \frac{\mathbf{M}_z - \mathbf{F}_y\ x_3}{L_{12}} \\
&\qquad \mathbf{F}_{z}^{mb1} = \frac{-\mathbf{M}_y - \mathbf{F}_z\ x_3 + (m_{carrier}\ g_z)\ \delta}{L_{12}}
\end{aligned} \tag{1}$$

MB2 reactions:

$$\begin{aligned}
&\text{using} \sum \mathbf{F} = \mathbf{0}: \\
&\quad \mathbf{F}_{ax}^{mb2} = |-\mathbf{F}_x - (m_{carrier}\ g_x)| \\
&\quad \mathbf{F}_{y}^{mb2} = (-\mathbf{F}_y - \mathbf{F}_y^{mb1}) \\
&\quad \mathbf{F}_{z}^{mb2} = -\mathbf{F}_z - \mathbf{F}_z^{mb1} + (m_{carrier}\ g_z)
\end{aligned} \tag{2}$$

On the other hand, mid-fidelity beam models, such as `OpenFAST-ElastoDyn` as in Liverud Krathe et al. (2025) or the structural solver `pyFrame3DD`, could be used to calculate the bearing forces and moments. However such methods are computationally too expensive for FLS constraint evaluation of the entire DLC matrix (size [~~72 000 × 10~~36 000 × 10]) in every iteration of a gradient-based optimizer.

The application of the above (conventional) analytical formulation for non-MR bearings (e.g. SRB; Eqs.1, 2) to those that physically reacts to moments (e.g. TRB2) was challenged by Stirling et al. (2021) where they showed, for a single-main-bearing

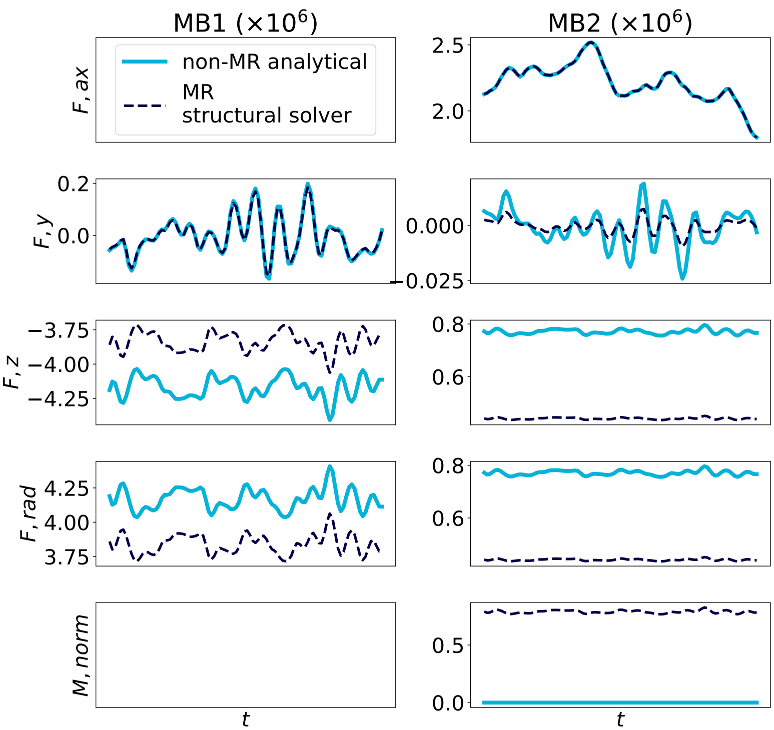

Figure 4. Bearing reactions comparison: pyFrame3DD with a moment-reacting MB2, and the conventional analytical formulation without a moment-reacting MB2

(SMB) configuration, that such a formulation highly overestimates the bearing reactions ($\mathbf{F}$) and proposed a bending-stiffness-based analytical moment-reacting (MR) model for such MR bearings, where the stiffness was calculated using a FE bearing model.

Extending their study for the double main-bearing configuration (DMB), similar results are found when bearing reactions are compared between `pyFrame3DD` structural solver's solution (with a moment-reacting MB2) and the conventional analytical formulation: Fig.4. At magnitudes of MN and MNm, these differences, especially in the radial reactions (F_{rad}), exponentially worsen the fatigue life (to the power of $p = 10/3$; Eq.25), hence requiring proportionally higher dynamic load capacities (C), but at the cost of higher bearing diameters and masses (Tab.3) to satisfy the fatigue constraints.

<u>Double-main bearing model with moment-reacting MB2</u>:

To this end, this work presents a **closed-form main bearing loads model** as follows, where the axially locating MB2 reacts

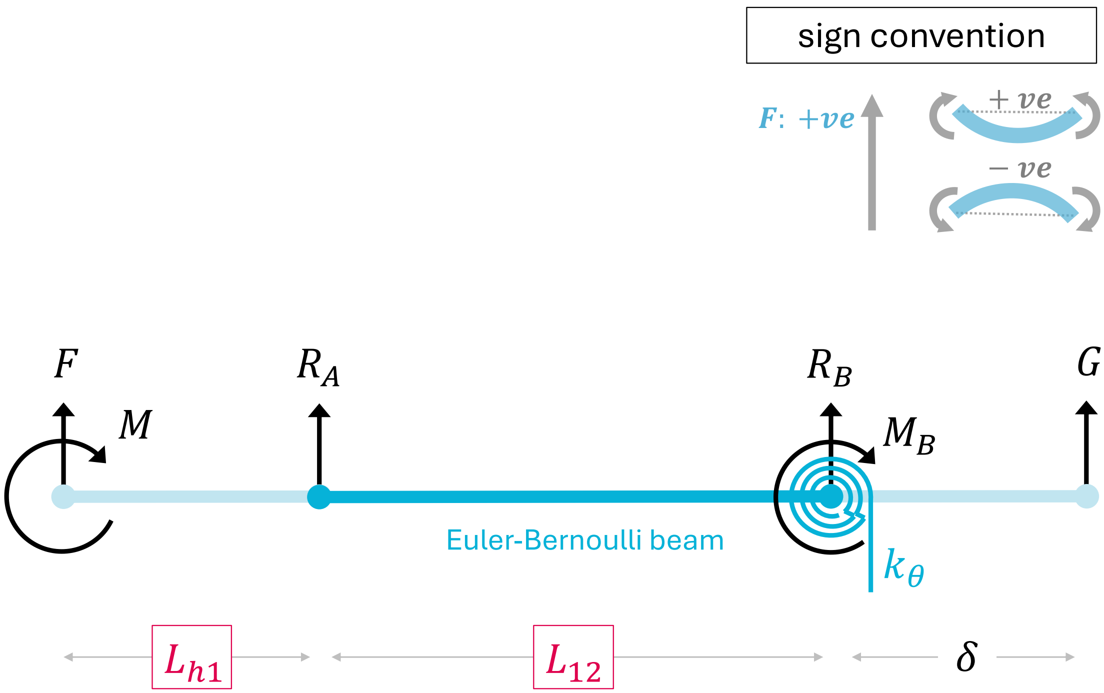

Figure 5. ~~MSA~~ MBSA with moment-reacting MB2, bearing-span modelled as EB-beam; in each plane

to moments (M_*^{mb2}) via the rotational spring (k_θ), through the relation $M_*^{mb2} = k_{**} \cdot \theta_*$, in the y- and z-directions and where θ is the slope/beam's cross-sectional rotation at the MB2-node. The relation is found through the Euler-Bernoulli (EB) beam (moment-slope) equation applied between the main-bearing span (L_{12}) with boundary conditions of 0-deflection at the MBs.

1. The EB-beam is assumed between the 2 MB-span (denoted A-B, Fig.5) to derive the slope (θ_B) relation with respect to forces and moments.

2. The full 2-bearing-shaft system with moment-reacting MB2 is reformulated, to derive bearing reaction forces and moments.

2.3.1 Slope at MB2 from first principles

Consider the shaft span between bearings A and B, of length L_{12}, modelled as an Euler–Bernoulli beam with constant flexural rigidity EI.

Let:

- $x = 0$ at bearing A (CRB),
- $x = L_{12}$ at bearing B (~~DTRB~~TRB2),
- R_A and R_B be the reactions (assumed +ve, vertical).

Since the left bearing (CRB) does not support moment,

$$M(0) = 0. \tag{3}$$

Internal Bending Moment: For a section at distance x from A, the only internal contribution is due to R_A:

$$M(x) = R_A x, \qquad 0 < x < L_{12}. \tag{4}$$

Beam Equation: From Euler–Bernoulli beam theory (and substituting $M(x) = R_A x$),

$$EI\, w''(x) := M(x) = R_A x. \tag{5}$$

First Integration (Slope): Integrating once:

$$EI\, w'(x) = \int R_A x \, dx = \frac{R_A x^2}{2} + C_1. \tag{6}$$

Second Integration (Deflection): Integrating again:

$$EI\, w(x) = \int \left(\frac{R_A x^2}{2} + C_1 \right) dx = \frac{R_A x^3}{6} + C_1 x + C_2. \tag{7}$$

Boundary Conditions (Assumed)
At $x = 0$ (bearing A), deflection is zero:

$$w(0) = 0 \quad \Rightarrow \quad C_2 = 0. \tag{8}$$

At $x = L_{12}$ (bearing B), deflection is also zero:

$$w(L_{12}) = 0. \tag{9}$$

Substituting:

$$\frac{R_A L_{12}^3}{6} + C_1 L_{12} = 0, \tag{10}$$

which gives

$$C_1 = -\frac{R_A L_{12}^2}{6}. \tag{11}$$

Slope at Bearing B: ~~The slope expression is~~ can be found by substituting Eqs.(11 and 8) in Eq.7:

$$EI\, w'(x) = \frac{R_A x^2}{2} - \frac{R_A L_{12}^2}{6}. \tag{12}$$

Evaluating at the location of bearing-B, i.e. $x = L_{12}$:

$$EI\,\theta_B = \frac{R_A L_{12}^2}{2} - \frac{R_A L_{12}^2}{6} \tag{13}$$

$$= \frac{R_A L_{12}^2}{3}. \tag{14}$$

Compatibility Relation ~~: Therefore,~~ is therefore obtained, which is the rotation at the ~~right bearing is~~second bearing (bearing-B):

$$\boxed{\theta_B = \frac{R_A L_{12}^2}{3EI}} \tag{15}$$

Bearing Constitutive Relation~~: The moment at the right bearing is~~, defines the relation between the rotation (θ) and moment (M) through the stiffness (k). To this end, the moment at bearing-B can be calculated using Eq.15:

$$M_B = k_\theta \theta_B$$

$$\boxed{M_B = \frac{k_\theta R_A L_{12}^2}{3EI}} \tag{16}$$

$$= R_A \cdot \lambda_L$$

where,

$$\lambda_L = \frac{k_\theta L_{12}^2}{3EI} = \lambda \cdot L_{12} \tag{17}$$

k_θ is the moment-reacting bearing's ~~rotational spring constant~~ tilting (or rotational) stiffness (in this plane)~~, and~~ ; the reader is referred to Sect.D for more details on its definition and estimation. λ_L is termed the compatibility term, representing the ratio of bearing rotational stiffness to the shaft bending stiffness.

To this end, the statically-indeterminate equations are now complete (with equal known-loads and unknown-reactions) to render bearing loads using shear force and bending moment equilibrium.

2.3.2 DMB-shaft model with MR-MB2

Consider, in each plane, a shaft supported by two bearings, with the concentrated forces and moments, as shown in Fig.5, with unknown reactions: $R_A, \quad R_B, \quad M_B$, and denoting $L = L_{h1} + L_{12} + \delta$ for the following discussion.

Global Equilibrium (involving only statics):

Using singularity functions (Budynas et al. (2021)) the shaft's shear force and bending moment equations can be determined.

~~**Global Equilibrium** (involving only statics):~~

~~Denoting $L = L_{h1} + L_{12} + \delta$,~~

Vertical Force Equilibrium: noting that the shear force outside the ~~MSA~~ MBSA should be zero i.e. $V(L^+) = 0$:

$$F + R_A + R_B + G = 0 \tag{18}$$

or

$$\boxed{R_B = -G - F - R_A} \tag{19}$$

Moment Equilibrium: noting that the bending moment outside the ~~MSA~~ MBSA should be zero i.e. $M(L^+) = 0$,

$$M + FL + R_A(L - L_{h1}) + R_B\delta + M_B = 0 \tag{20}$$

Substituting Eq.16 and Eq.19 in Eq.20, and collecting terms in R_A we get,

$$\boxed{R_A = \frac{-M - Fx_3 + G\delta}{L_{12}(1+\lambda)}} \tag{21}$$

defining the numerator as C,

$$C = -M - Fx_3 + G\delta$$

$$\text{then, } R_A = \frac{C}{L_{12}(1+\lambda)}$$

Therefore, the **new formulation of planar bearing loads for a double MB model with moment-reacting MB2** is given by the equation system, Eqs.(16, 19 and 21).

Limiting Cases:

1. Case: $k_\theta = 0$ (No Moment Resistance): $R_B = \frac{C}{L_{12}}$. The system reduces to a statically determinate beam (simply supported result).
2. Case: $k_\theta \to \infty$ (Rigid Moment Support): The denominator grows large and the system approaches fixed-end beam behaviour at bearing B.

2.3.3 Solving for each plane

As shown in Fig.6, ~~when the~~ the new planar equation system from Sect.2.3.2 is solved in the:

- **a**-plane: $\mathbf{F}_x^{mb1} = 0$ and $\mathbf{F}_x^{mb2} = |-\mathbf{F}_x - (m_{carrier}\ g\ \sin\phi)|$
- **b**-plane: $R_A = \mathbf{F}_y^{mb1}$, $R_B = \mathbf{F}_y^{mb2}$, and $M_B = \mathbf{M}_z^{mb2}$.
- **c**-plane: $R_A = \mathbf{F}_z^{mb1}$, $R_B = \mathbf{F}_z^{mb2}$, and $M_B = \mathbf{M}_y^{mb2}$.
- ~~**a**-plane:~~ $\cancel{\mathbf{F}_x^{mb1} = 0}$ ~~and~~ $\cancel{\mathbf{F}_x^{mb2} = |-\mathbf{F}_x - (m_{carrier}\ g\ \sin\phi)|}$

with bearing axial ($\mathbf{F}_x$) and radial ($\mathbf{F}_y$, $\mathbf{F}_z$) loads calculated for both bearings.

Thereafter, radial loads $\mathbf{F}_{rad}$ are accumulated as follows:

$$\mathbf{F}^*_{rad} = \sqrt{(\mathbf{F}^*_y)^2 + (\mathbf{F}^*_z)^2}$$

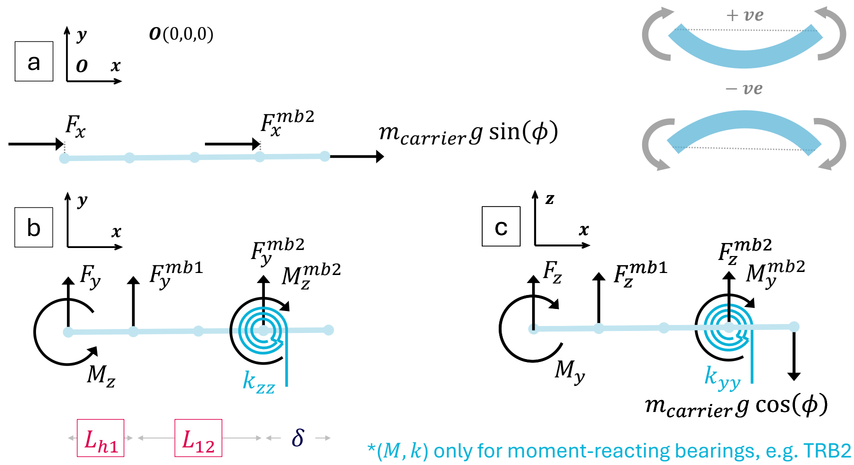

Figure 6. Free-body diagram of main-shaft static equilibrium in the local (hub) coordinate system;
a: x-plane, **b**: yx-plane, **c**: zx-plane; *top-right*: bending moment convention.

Also, the absolute value operation of the axial force on the locating bearing (MB2) is noted from the above implementation:
$\mathbf{F}_x^{mb2} = |\dots| = \text{abs}(\dots)$.

The locating bearing always reacts to the magnitude of axial force, regardless of sign. The sign is relevant for internal stress direction, but $\mathbf{P}$ (equivalent bearing load) is always positive in life/fatigue calculations. In other words, whether axial tension or compression, the bearing 'reacts' to the load regardless. Therefore, $|\dots|$ is physically consistent with bearing reactions, as well as gradient calculations because $\mathbf{F}_x^{mb2}$ is independent of the design variables (its partial derivative is $\mathbf{0}$).

The resulting bearing reactions using this formulation are validated in Sect.4.1.

2.4 Bearing ~~Fatigue-life~~ Fatigue-Life Constraints

2.4.1 Empirical relations of bearing properties ~~and~~ with its bore diameter

The variation of bearing properties with respect to its (bore) diameter (Tab.3) is shown in Fig.7. To account for the bearing housing's mass, the total bearing mass is incremented by an empirical housing factor of $(80/27)$ (NLR (2026)).

The empirical bearing property database is supplemented in the bearing component at the class level, facilitating implementation of its partial derivatives with respect to the design variables (i.e. D). The supplied partial derivatives are verified against the complex-step method - making sure the derivates' float representations are not hindered by subtractive cancellation - thereby rendering gradients to machine-zero precision.

Table 3. Bearing property estimations with respect to its bore diameter 'D' – for heavy load cases; *-code enhancements.

Name	**Type**	$\delta_{ang,max}$ [deg]	**Face width** [m]*	**Mass** [m]	C [kN]*	**r***
CARB	Non-MR	0.5	$0.4299\ D + 0.0382$	$3,682.8\ D^{2.7676}$	$16,676.0\ D^{1.4746}$	$[0,1,1,0,0,0]$
CRB	Non-MR	0.04 - 0.06	$0.157\ D + 0.0849$	$1,070.8\ D^{1.8278}$	$4,526.5\ D^{0.9556}$	$[0,1,1,0,0,0]$
SRB	Non-MR	1.5 - 3.0	$0.2463\ D + 0.185$	$2,688.3\ D^{1.8877}$	$13,878.0\ D^{1.0796}$	$[1,1,1,0,0,0]$
SRB_NL	Non-MR	1.5 - 3.0	$0.2463\ D + 0.185$	$2,688.3\ D^{1.8877}$	$13,878.0\ D^{1.0796}$	$[0,1,1,0,0,0]$
TRB	MR	0.03 - 0.07	$0.1499\ D$	$543.01\ D^{1.9043}$	$1,993.8\ D^{0.318}$	$[1,1,1,0,1,1]$
TRB2*	MR	0.02 - 0.06	$0.1541\ D + 0.2087$	$1,442.6\ D^{1.8932}$	$6,579.9\ D^{0.8592}$	$[1,1,1,0,1,1]$

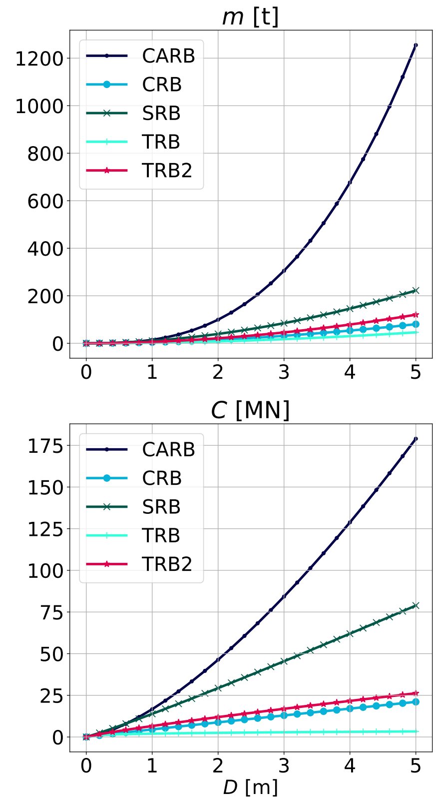

Figure 7. Bearing properties (mass and C) with respect to bearing bore diameter

From the right plot in Fig.7, the high dynamical load capacity (C) of CARB and SRB type bearings can be seen. More specifically, to reach $C = 20$MN, CARB must be only 1 m in diameter, compared to almost 4 m needed for a TRB2. This allows setups with CARB and SRB to satisfy the FLS-life constraint already at a lower diameter, or at lower masses, compared to setups with a TRB2. The discussion here revolves around only two objectives: minimum mass and a satisfied FLS-life constraint. In reality, practical implications such as axial displacements, bearing roller load distribution, ~~MSA~~ MBSA load paths and isolation from the gearbox, etc., govern the setup's failure rate and reliability.

2.4.2 Equivalent bearing loads (P)

Equivalent bearing loads can be calculated, according to ISO (2007), as in Eq.22.

$$\mathbf{P} = X\mathbf{F}_{rad} + Y\mathbf{F}_x \tag{22}$$

with the dynamic load factors ($X,\ Y$) from Tab.4.

Table 4. Dynamic load factor values (X,Y) for double-row radial roller bearings

	$F_{ax}/F_{rad} \leq e$	$F_{ax}/F_{rad} > e$
	light, $(\cdot)_1$	*heavy*, $(\cdot)_2$
X	1	0.67
Y	$0.45\cot\alpha$	$0.67\cot\alpha$

2.4.3 Weighted-averaged fatigue equivalent loads (P)

There are 2 ways to aggregate bearing equivalent load time series across all wind speeds "$\mathbf{P}$" to a weighted-averaged scalar equivalent load "P", i.e. $\mathbf{P} \rightarrow P$, in order to formulate the bearing life constraint:

1. LRD (Load Revolution Distribution):
It is the conventional method of time-series `histogram`-bin counting of loads ($\mathbf{P}$) and corresponding rotational speeds ($\mathbf{\Omega}$); the reader is refereed to the wind turbine standard IEC (2012) for more details on its computation.

2. DEL (Damage Equivalent Load):
The full raw time series of main bearing equivalent loads ($\mathbf{P}$) is reduced into the fatigue relevant metric 'DEL'. First, the vector of DEL for all wind speeds is calculated using Eq.23.

$$\mathbf{p}_{DEL} = \left(\frac{\sum_i (\mathbf{P}^p \odot \mathbf{N})}{\mathbf{n}}\right)^{1/p} \; ; \; \mathbf{N} = \frac{\mathbf{\Omega}}{60} \cdot \Delta t \; ; \; \mathbf{n} = \sum_i \mathbf{N} \tag{23}$$

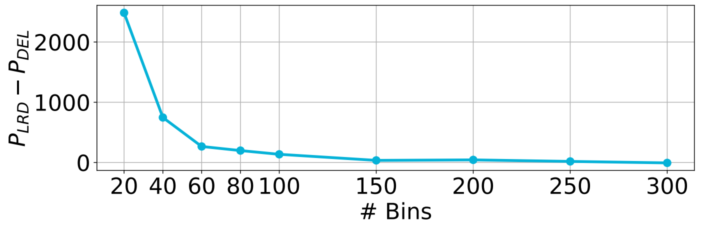

Figure 8. Comparing methods to aggregate bearing equivalent load time series: DEL and ~~LDD~~LRD

where, $\mathbf{\Omega} = \Omega_{i,j}$ is the matrix of rotational speeds for the entire DLC, $\Delta t = t_2 - t_1$ is the (constant) time step, $\mathbf{n}$ is total number of revolutions in the time series, $\sum_i$ is sum-over-rows resulting in a vector of length n_{ws} (number of wind speeds), and $\odot$ is element-wise (or Hadamard) product of two matrices.

Furthermore, $\mathbf{p}_{DEL}$ is weighted by the wind speed probability $\mathbf{p}_u$ and combined into a single aggregate fatigue metric:

$$P_{DEL} = \left(\sum_J (\mathbf{p}_{DEL}^p \odot \mathbf{p}_u) \right)^{1/p} \tag{24}$$

A validation of the analytical method of DEL shows that it corresponds to the converging value of an equivalent bin-counting ~~LDD~~ LRD algorithm, Fig.8. This can also be understood when one sees the DEL-formulation counting the bins with bin-width being the (simulation) time step (Δt) or the number of bins being the total number of (simulation) time steps (~~$(\sum j) - 1 = 72\,000 - 1$~~$(\sum j) - 1 = 36\,000 - 1$).

2.4.4 Fatigue life equation (L_{10})

It can be calculated, according to ISO (2007), as in Eq.25.

$$\begin{aligned} L_{10,rev} &= \left(\frac{C}{P}\right)^p \cdot 10^6 \\ p \text{ (fatigue exponent)} &= \begin{cases} \frac{10}{3} & : \text{roller bearing} \\ 3 & : \text{ball bearing} \end{cases} \\ L_{10,hrs} &= \frac{L_{10,rev}}{n_0 \cdot 60} \end{aligned} \tag{25}$$

where n_0 [rpm] is the rated rotational speed of the rotor/main shaft.
Future work entails utilizing ($a_{\text{ISO}}\ a_e$) for the modified life equation (L_{nm}), Ishihara et al. (2025).

The L_{10}-life in WTMBs is based on certain assumptions (Hart et al. (2020)), from them being: 1. Condition of elasto-hydrodynamic lubrication (EHL) is satisfied throughout the bearing lifetime, 2. Steady-state operation, i.e. not taking into account intermittent operational conditions, 3. Presence of wear instead of, or alongside rolling contact fatigue (RCF) is not accounted for.

The 2 methods of ~~LDD~~ LRD and DEL render two ways to calculate bearing life:

LRD based:

$$L_{10,rev}^{LRD} = \left(\frac{C}{P_{LRD}}\right)^{p} \cdot 10^{6} \tag{26}$$

DEL based:

$$L_{10,rev}^{DEL} = \left(\frac{C}{P_{DEL}}\right)^{p} \cdot 10^{6} \tag{27}$$

In light of efficient optimization of fatigue-driven components, utilizing full time-series non-smooth bin-counting (Eq.26) is shown in (Gupta and Nejad (2026)) to render convergence issues. Instead analytical DEL-based fatigue-life constraints (Eq.27) render efficient and robust optimization.

2.5 Shaft Structural Model

Conventional models define the main-shaft ULS criterion using low-fidelity analytical formulations (Guo et al. (2015b), Eq.(2.19-20)) to calculate loads (forces and moments) and subsequent (von-Mises) stresses in the main-shaft elements (Budynas et al. (2021), Eq.5-15).

In this study, a more structurally sound and physically consistent stiffness-based 3-dimensional shaft structural model is utilized for the LSS ULS constraints formulation, numerically implemented in `WISDEM` using the mid-fidelity ~~`Frame3DD`~~`pyFrame3DD` library, and based on the stress formulation in Appendix Sect. C~~)~~. The LSS, along with other drivetrain structural components like HSS and bedplate, is modelled with 3D Timoshenko beam elements~~and~~ , which includes shear deformation and geometrical stiffness effects~~. The~~ , bearings' support reactions (for the fixed and floating MBs) and their deflections through the bedplate. Hence, the model enhances design accuracy and setup validity, matching real drivetrain physics better compared to the ~~the~~ low-fidelity analytical equations.

With reference to the present moment-reacting-MB2 ~~MSA~~ MBSA setup, a statically indeterminate system is created, which can not be solved using only static equilibrium equations and (bearing) stiffness must be taken into account. The structural solver `pyFrame3DD` advantageously handles and solves such models through stiffness-deformation compatibility (direct stiffness and mass assembly) that replaces equilibrium.

3 Constraint Gradient-based Optimization

3.1 Overview

The constraint gradient-based optimization problem with a single objective can be formulated as in Eq.28.

$$\begin{aligned}
\text{find} \quad & \mathbf{d}^* \\
\text{which minimizes} \quad & f(\mathbf{d}) \\
\text{subjected to} \quad & \mathbf{g}(\mathbf{d}) < 0 \\
& \mathbf{h}(\mathbf{d}) = 0 \\
& \mathbf{d} \in \left[\mathbf{d}^{\mathrm{lb}}, \mathbf{d}^{\mathrm{ub}}\right]
\end{aligned} \tag{28}$$

where f is the objective function, and 'lb' and 'ub' represent the lower and upper bounds, respectively.

Table 5. Optimization driver options

Optimizer option	Value
Optimizer	`SLSQP`
Tolerance	10^{-6}
Maximum iterations	20

An eXtended Design Structure Matrix (XDSM) diagram, describing the flow of data variables and sequence of module (drivetrain component) execution, of the present multidisciplinary optimization problem, is shown in Fig.9. The optimizer options are presented in Tab.5.

3.2 Objective function (f)

The present work investigates weight-optimization of critical drivetrain components while preserving critical bearing fatigue metrics.

Barter et al. (2023) analysed 30 large ($15-25$MW) FOWT DT concepts numerically (using NLR's `WEIS` toolset) and concluded that, unlike fixed-bottom WTs that showed relatively flatter mass-LCOE landscape, floating concepts showed greater dependency on and benefit with a lighter rotor-nacelle assembly (RNA). It is concluded that the impact of an optimal drivetrain design is threefold: (1) Tower-top mass and inertial loads contribute towards support-structure design, (2) Weight-based cost contributions to turbine CapEx in LCOE, and (3) Contribution to overall electro-mechanical reliability and efficiency.

Therefore, the primary objective is to minimize the mass of the main ~~shaft~~ bearing-shaft assembly, which includes the low-speed shaft (LSS) and the two MBs: $f = (m_{MSA} + m_{mb1} + m_{mb2})$.

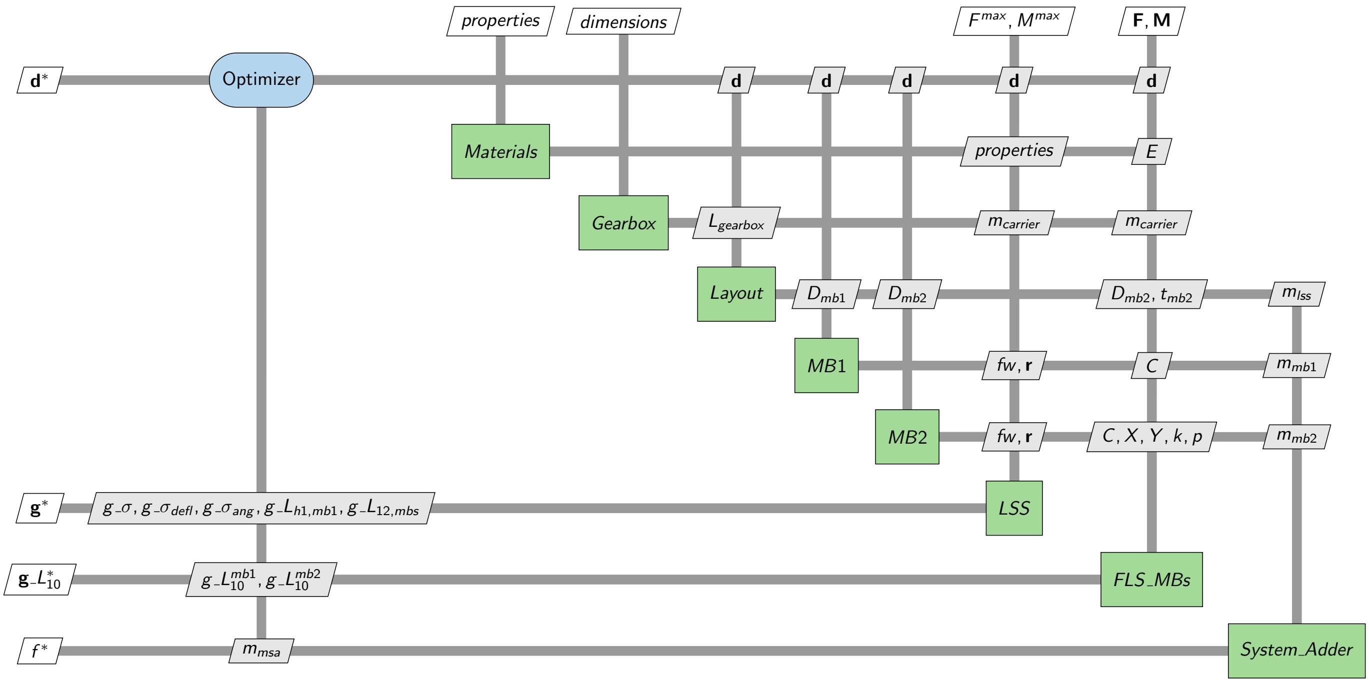

Figure 9. XDSM diagram of the main-shaft assembly optimization problem

3.3 Design Variables (d)

The design variables used are listed in Tab.6, and are those marked red in Fig.10.

Table 6. Design variables for ~~MSA~~ MBSA design optimization

d	symbol	type	lb	ub	[units] description
d_1	L_{h1}	float	0.1	5.0	[m] distance between hub-LSS input and MB1
d_2	L_{12}	float	0.1	8.0	[m] distance between MB1 and MB2
d_3	D_{lss}	array[2]	1.0	5.0	[m] diameters of LSS shaft ends
d_4	t_{lss}	array[2]	$4 \cdot 10^{-3}$	0.5	[m] thicknesses of LSS shaft ends

3.4 Inequality Constraints (g)

The constraints used are listed in Tab.7, and are those marked red in Fig.11.

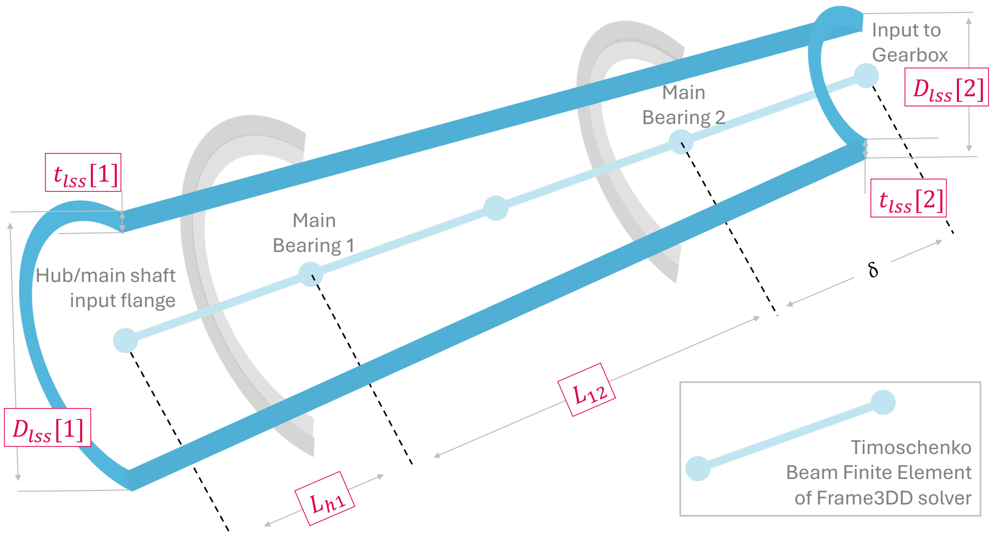

Figure 10. Design variables of the main-shaft assembly

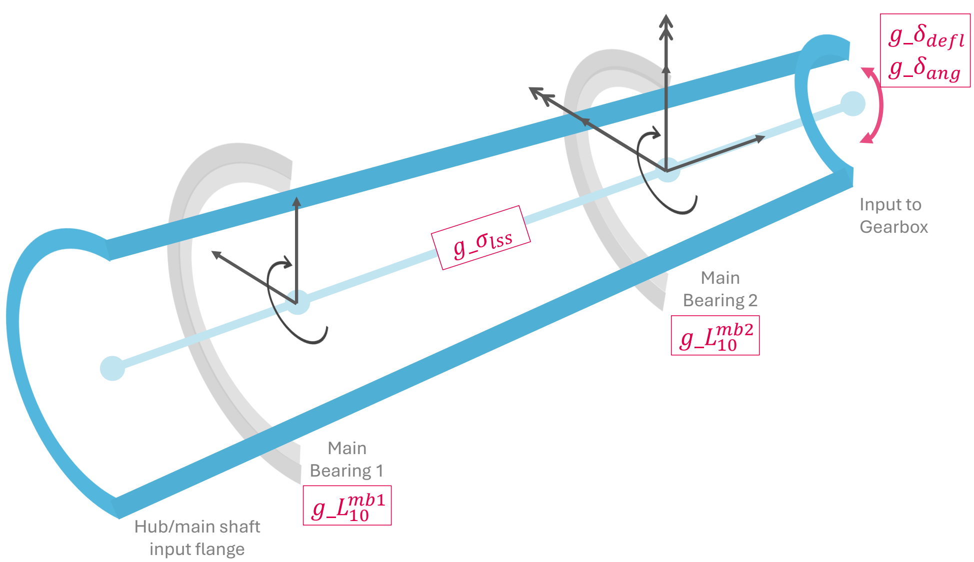

Figure 11. Inequality constraints on the main-shaft assembly

Table 7. Constraints for LSS design optimization;
(*Abbreviations:* DW = downwind, GB = gearbox, DT = drivetrain, TT = tower-top).

g(d)	symbol	type	bound	description
g_1	σ_{lss}	array[4]	≤ 1.0	ratio of von-Mises stresses in shaft elements to that permissible (Eq.C3)
g_2	δ_{defl}	float	≤ 1.0	ratio of deflection at the LSS-end (GB input) to maximum permissible ($\delta_{defl,\ max}$)
g_3	δ_{ang}	float	≤ 1.0	ratio of angular deflection at the LSS-end (GB input) to maximum permissible ($\delta_{ang,\ max}$)
g_4	$L_{h1,mb1}$	float	≥ 0.0	L_{h1} should be greater than half of MB1 face width
g_5	$L_{12,mbs}$	float	≥ 0.0	L_{12} should be greater than half of the sum of MB face widths
g_6	L_{10}^{mb1}	float	≥ 1.0	L_{10}-life of MB1 should be more than design life
g_7	L_{10}^{mb2}	float	≥ 1.0	L_{10}-life of MB2 should be more than design life

The von-Mises stress constraint is calculated as in Eq.29:

$$g\_\sigma_{lss} = \frac{\gamma \cdot \sigma_v}{\sigma_{yield}} \tag{29}$$

where σ_v is the vector of von-Mises stresses in each discretized element of the LSS (Eq.C3) and $\gamma = \gamma_f \cdot \gamma_n \cdot \gamma_m$, the total partial safety factor (SF), Tab.B1.

The MB FLS life constraint can be defined as in Eq.30, where the L_{10}-life of the main bearings (L_{10}^{mb*}) should exceed the total design life of the bearing or the wind turbine.

$$g\_L_{10}^{mb*} = \left(\frac{L_{10,hrs}}{L_{design,hrs}}\right)^{1/p} = \left(\frac{L_{10,hrs}}{L_{design,yrs} \cdot 8766}\right)^{1/p} \tag{30}$$

4 Discussion of Results

4.1 Analytical moment-reacting ~~MSA~~ MBSA model

~~To verify the analytical formulation ,~~ The proposed EB-beam-based formulation for bearing loads (Eq.(16, 19 and 21); in Sect.2.3.2), is verified against an equivalent mid-fidelity beam finite-element structural model of the main-bearing-shaft assembly, which was created using the `pyFrame3DD` ~~structural model~~framework, with nodes, forces and reactions as shown in Fig.2.

Non-moment reacting (non-MR) MB2

~~With~~ For the limiting case of $k_\theta = 0$ ~~, as defined in Sect.2.3.2, the~~ (i.e. the second main bearing MB2 no longer reacting

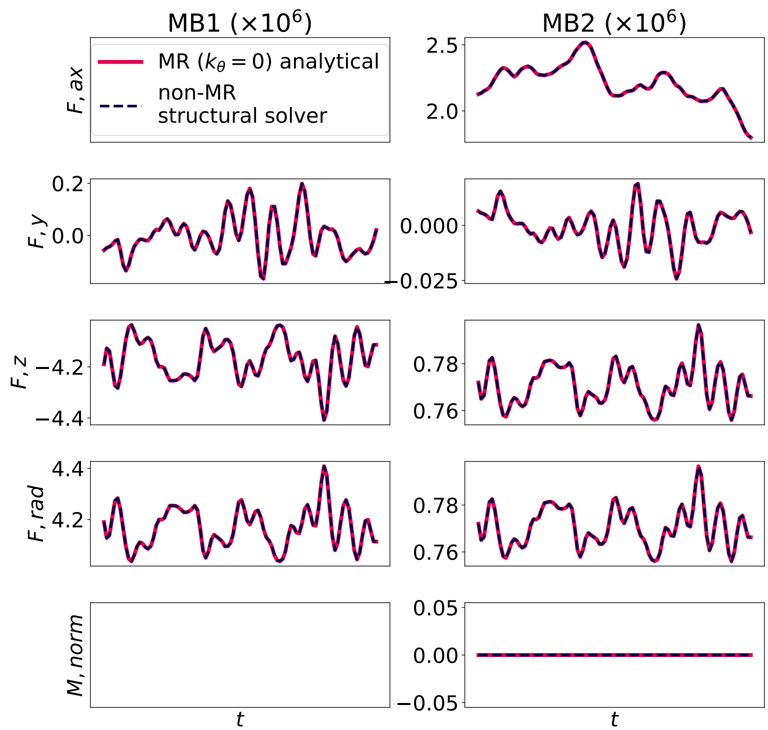

Figure 12. Non-moment-reacting MB2: comparing bearing reactions from the structural solver and the analytical EB-beam formulation (with $k_\theta = 0$)

to moments), the proposed bearing loads formulation renders the conventional non-moment reacting MB2 setup ~~is rendered~~ ~~(~~(defined in Eqs.1, 2), which ~~is~~ exactly matches with the bearing reactions resulting from the equivalent structural beam solver, as illustrated in Fig.12. It also be observed, from the right-bottom subplot, that the reaction from MB2 for moment loads is zero (M, norm $= 0$), i.e. it is not supporting moments.

Moment-reacting (MR) MB2

With MB2 now reacting to moments ($k_\theta \neq 0$), Fig.13 compares the bearing reactions ~~between~~ resulting from the mid-fidelity structural solver and the proposed EB-beam-based formulation~~from Sect. 2.3.3.~~.

Firstly, it can be observed, from the right-bottom subplot, that setting MB2's rotational stiffness to non-zero ($k_\theta \neq 0$) and to its estimated value allows MB2 to react to the moment loads acting on it, i.e. (M, norm $\neq 0$).

Additionally and more importantly, for all the loads the bearings support (axial, radial and moment), the proposed formulation is seen to match very well with results from the structural solver. Tab.8 lists the maximum absolute percentage (MAP) error (Eq.E1) for the different main bearing reactions, where $M^{mb2}_{norm} = \sqrt{(M^{mb2}_y)^2 + (M^{mb2}_z)^2}$. The bearing loads being at the scale of (10^6), the maximum error observed is only about 0.28%, validating and giving confidence in the proposed bearing loads formulation.

Table 8. Error on MR bearing loads between structural solver and analytical EB-beam formulation; corresponding to Fig.13

Reaction	% Error (MAPE)
F^{mb1}_{rad}	0.024
F^{mb2}_{ax}	0.0
F^{mb2}_{rad}	0.213
M^{mb2}_{norm}	0.28

4.2 Design Optimization of the Main-Shaft Assembly

4.2.1 Variable convergence and limit-state comparison

~~MSA~~ MBSA design variable optimization convergence in shown in Fig.14, while the optimal design is listed in Tab.9. To converge from a given set of initial conditions far from the minima, the design optimization of 6 design variables under 7 constraints took ~~$\approx$ 15 s, 16 iterations, 19~~ $\approx$ 12 s, 13 iterations, 22 function evaluations and ~~16~~ 13 gradient evaluations. At the optimal design, all constraints are satisfied, while the shaft stress and bearing fatigue-life constraints are active.

According to IEC (2012) (61400-4), the MBs should exceed a life of 100 000 hours for a design lifetime of 20 years, and the former (life in hours) should be adjusted for a different design lifetime, e.g. 219150 hours for 25 years lifetime.

It can be noted from Tab.9 that considering only ULS constraints for mass minimization, as currently present in `DrivetrainSE` used to design the IEA 15MW turbine and drivetrain, does not render a reliable design in terms of critical bearing fatigue, wherein the evaluated L_{10}-life in hours was only 5.3 and 13.9 for MB1 and MB2 respectively, compared to 219150.0 hours when the constraints are augmented with fatigue-life constraints for each bearing. This in turn shows that these type of machines are highly and critically driven by fatigue, negligence of which results in severe under-design.

4.2.2 Advantage of analytically-differentiable bearing fatigue formulation

Multiple sets of initial conditions (ICs) were chosen to showcase their effect on optimization convergence, as listed in Tab.10. L_{h1} and L_{12} (segment lengths of the main shaft) are varied, on a grid between their bounds.

Formulating the bearing fatigue constraint through DELs (Eq. 24) is considered, which are:

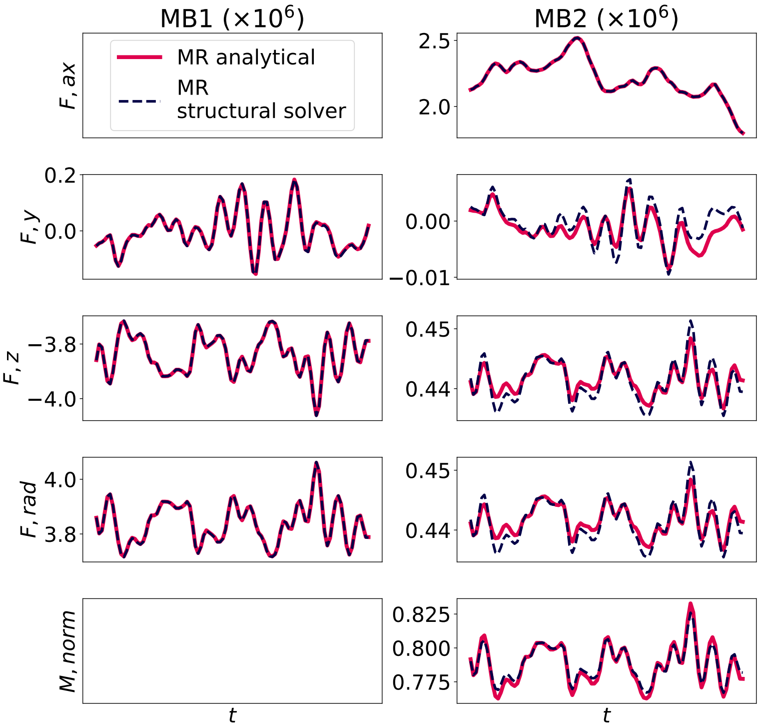

Figure 13. Moment-reacting MB2: comparing bearing reactions from the structural solver and the proposed analytical EB-beam formulation (with $k_\theta \neq 0$)

1. Smooth and analytically differentiable: analytical gradients are critical for convergence of gradient-based optimizers.
2. Computationally cheap: avoiding full DLC time-series `histogram`-bin-counting within the optimization loop.

By using smooth DEL constraints, the robustness within optimization is evident (Fig.15) by the consistent convergence irrespective of widely different initial conditions – an indicator of potentially finding a global minimum.

4.2.3 Parametric study on viable main-bearing setups

Potentially viable main bearing combinations were varied between sets defined in Tab.11, their performance trade-offs were accessed and the converged design values were recorded; all other design variables and input parameters were kept unchanged.

Table 9. Results from ~~MSA~~ MBSA design optimization; ()*-only evaluated, not included in optimization.

d, g, f	Converged value	
	ULS only	ULS+FLS
L_{h1}	0.149	~~0.310~~ 0.426
L_{12}	0.354	~~1.721~~ 4.370
D_{lss}	[1.438, 1.284]	[~~3.440, 3.204~~2.115, 4.216]
t_{lss}	[0.004, 0.510]	[~~0.087, 0.082~~0.114, 0.008]
$\max(g(\sigma_{lss}))$	1.0	~~0.99~~ 1.0
$g(L_{10}^{mb1})$	(0.041)*	1.0
$g(L_{10}^{mb2})$	(0.055)*	1.0
m_{MSA}	23 095	~~110 409~~ 120 341

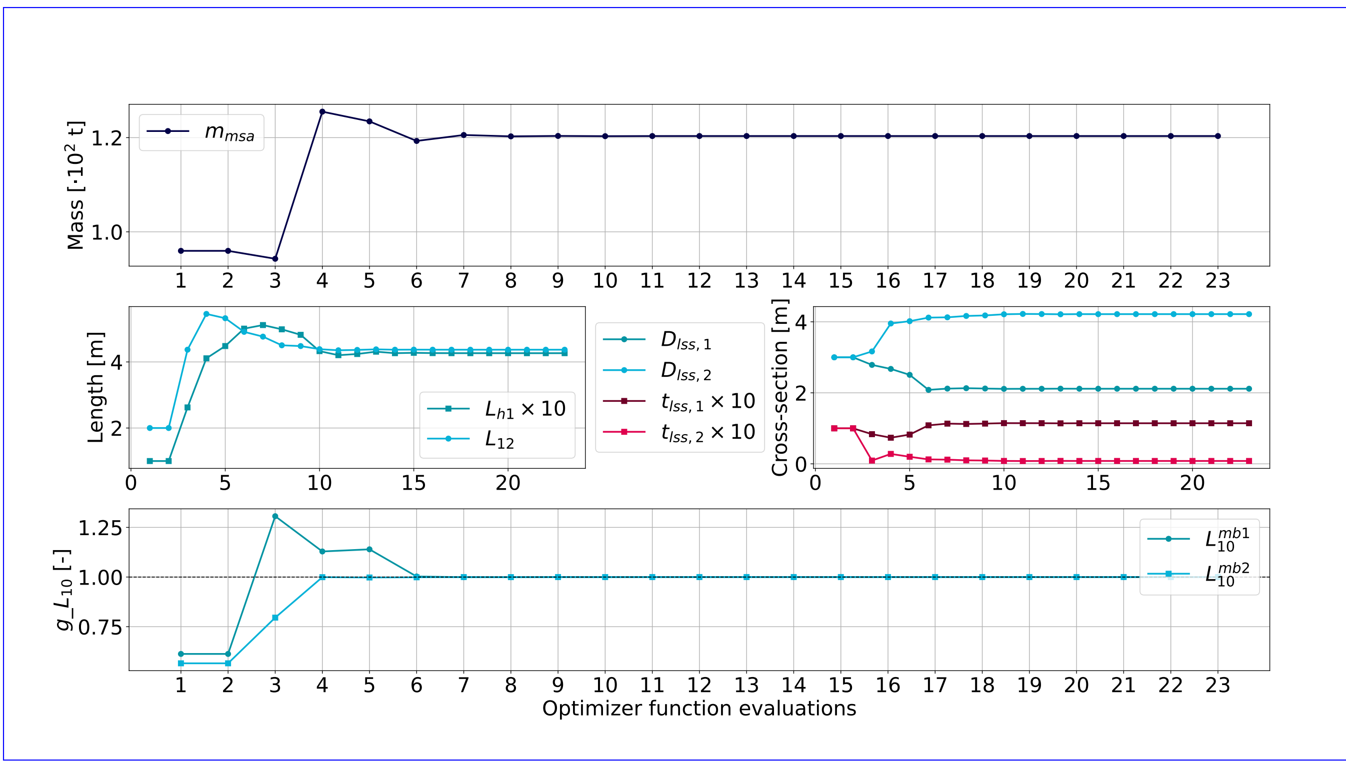

Figure 14. Convergence plot of optimization variables with iterations

Table 10. Initial conditions (ICs)

d / Set	1	2	3	4
L_{h1}	1.25	3.75	1.25	3.75
L_{12}	2.0	2.0	6.0	6.0

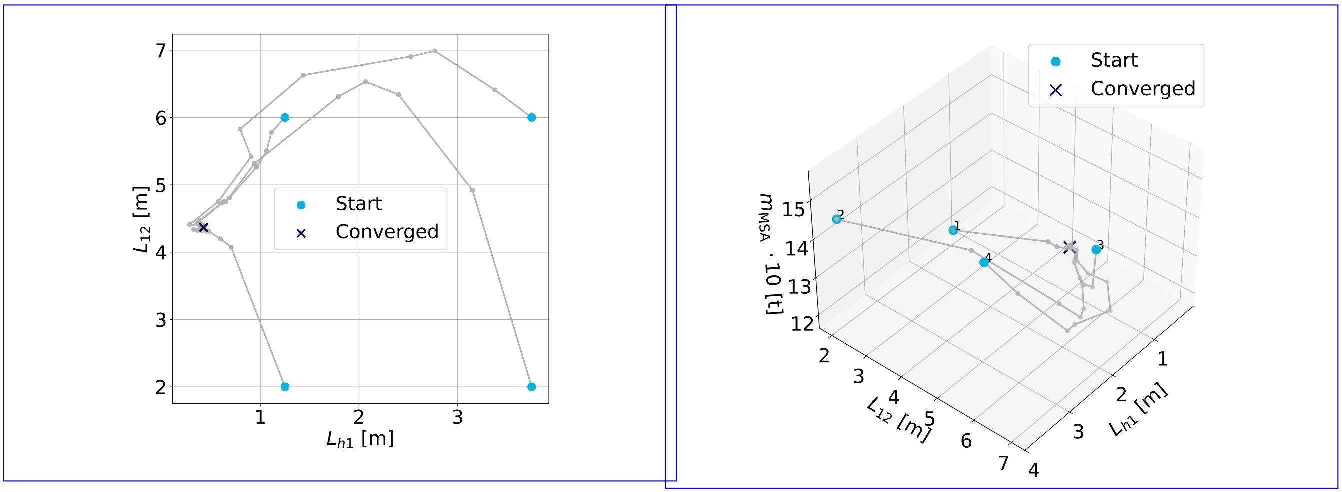

(a) 2D landscape with design variables (lengths-L_*) on the x,y-axis (b) 3D landscape additionally with objective (mass-m) on the z-axis

Figure 15. Smooth DEL-based constraint: optimization path and robust convergence.

The optimization results demonstrate a strong dependency of the drivetrain system mass on the main bearing configuration and load transfer mechanism.

Geometric design variable comparison, Fig.16:

To enable direct interpretation of how each design variables (geometric parameter) responds to changes in bearing configuration, each geometric parameter is presented in an individual subplot, and colours indicate different bearing arrangements.

The figure highlights how bearing-combination choices influences shaft geometry, particularly diameter and wall thickness, reflecting different load transfer mechanisms.

System component mass distribution, Fig.17:

The optimized mass distribution reveals that the dominant contributor to total mass depends strongly on the bearing configuration.

The lowest total system mass (~~98 t~~82 t) is achieved for the ~~CRB~~SRB+SRB configuration, approximately ~~48% reduction~~ 53% lighter compared to the heaviest CARB+~~SRB~~ TRB2 design. Mass-efficiency is attributed to the relatively high dynamic load capacity of SRB at low bearing diameter (Fig.16) and masses.

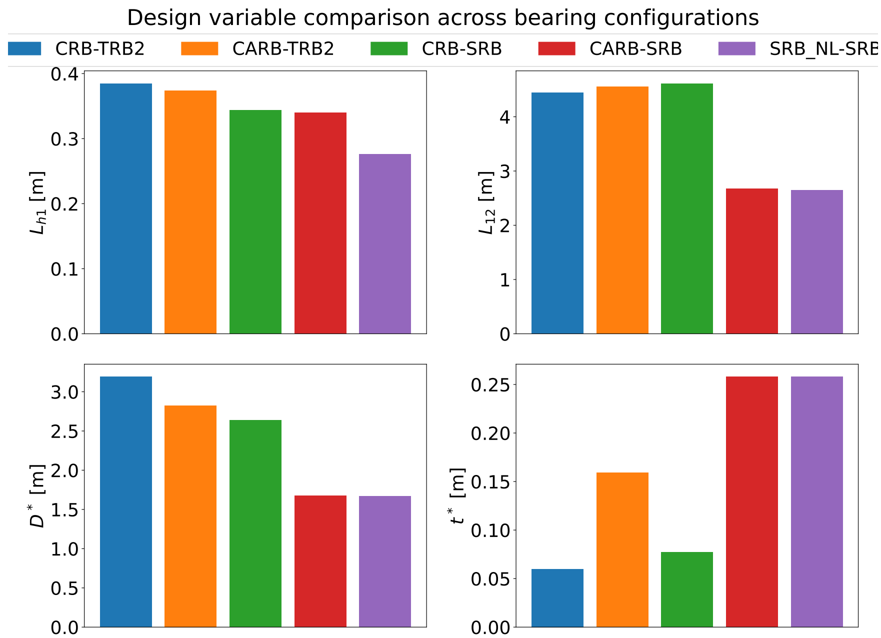

Figure 16. Comparison of optimized design variables for different main bearing configurations; $()^*$ indicates mean values.

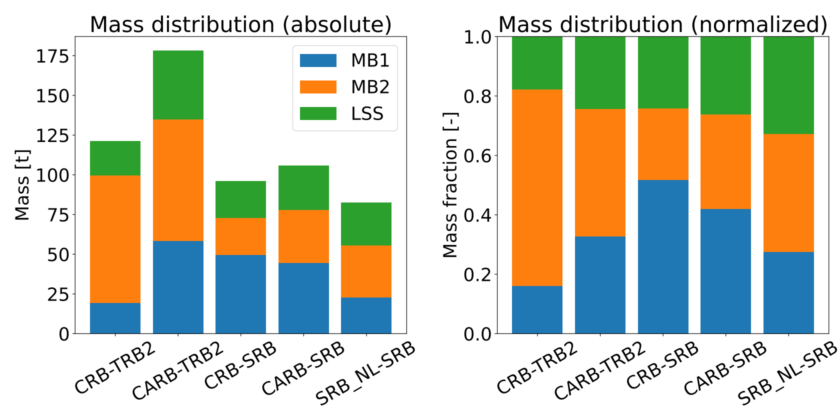

Figure 17. System mass distribution across different main-bearing configuration setups

Table 11. Design optimization on different main bearing configurations

height-	Moment-reacting setups		Non-moment-reacting setups	
d, g, f	**Set 1**	**Set 2**	**Set 3**	**Set 4**
-	CRB + TRB2	CARB + TRB2	CRB + SRB	CARB + SRB
L_{h1}	~~0.310~~ 0.425	~~0.438~~ 0.373	~~0.314~~ 0.336	~~0.449~~ 0.340
L_{12}	~~1.721~~ 4.368	~~2.153~~ 4.531	~~3.077~~ 4.538	~~2.623~~ 2.679
D_{lss}	[~~3.440,3.204~~2.115,4.217]	[~~1.686,3.552~~1.462,4.177]	[~~3.681,1.021~~3.906,1.264]	[~~2.046,1.699~~1.452,1.
t_{lss}	[~~0.087,0.082~~0.114,0.008]	[~~0.466~~0.314,0.004]	[~~0.059,0.428~~0.038,0.121]	[0.5,0.015]
g_σ_{lss}	[~~0.26,0.99,0.99,0.76~~0.388,1.0,0.908,1.0]	[~~0.45,0.80,0.80,1.0~~0.288,0.493,0.577,0.99]	[0.489,1.0,1.0,0.996]	[0.530,1.0,~~0.81~~1.0,1.
g_δ_{ang}	0.0	0.0	~~0.282~~ -0.263	~~0.283~~ -0.264
g_δ_{defl}	0.003	0.003	~~0.99~~ 1.0	0.99
$g\_L_{10}^{mb1}$	1.0	~~3.05~~ 2.984	1.0	~~2.945~~ 1.549
$g\_L_{10}^{mb2}$	1.0	1.0	~~1.06~~ 1.0	~~1.349~~ 1.027
m_{mb1}	~~39 977~~ 19 203	~~92 867~~ 58 376	~~41 167~~ 47 319	~~99 742~~ 44 451
m_{mb2}	~~53 281~~ 79 585	~~53 267~~ 76 163	~~19 122~~ 23 195	~~30 578~~ 33 452
m_{lss}	~~17 151~~ 21 552	~~34 692~~ 42 946	~~38 119~~ 23 228	~~60 492~~ 27 734
f	~~110 409~~ 120 341	~~180 828~~ 177 486	~~98 409~~ 93 743	~~190 813~~ 105 638

CARB-based configurations consistently result in significantly higher total mass~~$(\approx 180 - 190\ t)$~~. This behaviour is attributed to the bearing's inherent heavy-weight property even at low diameters. On the other hand, CRB-based solutions enable a more balanced mass allocation between bearings and the shaft.

Moment-reacting (TRB2-based) systems exhibit reduced ~~shaft mass due to~~ MB1 and LSS masses due to the internal moment support ~~within the bearing arrangement~~by the second MR-bearing, hence relieving shaft loads. However, this advantage is slightly offset by increased ~~bearing mass, due~~ MB2 mass, attributed to the need for higher bearing capacity (at higher bearing diameters) to satisfy equivalent fatigue-life constraints, leading to marginally sub-optimal total system mass compared to the ~~optimally~~ lightest configuration.

Non-linear constraint utilization heatmap, Fig.18:

The constraint utilizations are shown as a heatmap across different bearing configurations, where a black dot highlights active constraints and ~~red~~ green indicates values approaching unity. This enables direct identification of governing constraints in each design optimization.

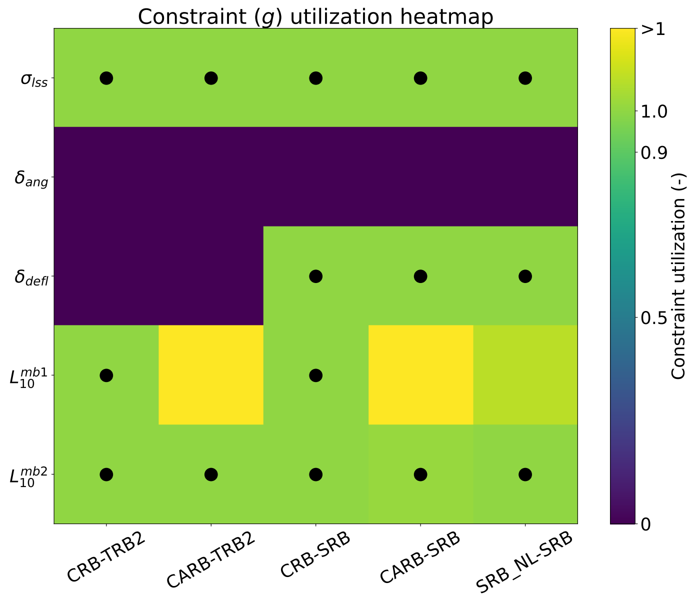

Figure 18. Constraint activity heatmap of design optimization across different main-bearing configuration setups

Investigating what drives the design and guides it to convergence, it can be seen that the ultimate shaft stresses are active $(\max(g\_\sigma_{lss}) \approx 1)$ in both ~~MSA~~ MBSA setup configurations. However, differences are seen when the bearing fatigue-life (g_L_{10}) and LSS end-deflections (g_δ_{defl}) are monitored. For MR setups, the fatigue lives are the design drivers. For non-MR setups on the other hand, the shaft deflections seem to in addition dictate the design. This can be related to the incapability of MB2 to react to tilting moments/NTLs, increasing bearing (axial and radial) loads and shaft loads (peaks and those carried through to GB-input), consequently, increasing the shaft end-deflection.

Trade-off comparison of total system mass and maximum constraint, Fig.19:

~~The Pareto~~ A Pareto-style trade-off plot demonstrates that CARB-based configurations are structurally inefficient, as they require significantly higher mass while still operating under active constraints. In contrast, CRB-based configurations achieve near-optimal constraint utilization at substantially lower system mass.

~~Geometric~~ Influence on total drivetrain design~~variable comparison~~~~, Fig.16: Comparison of optimized design variables for different main bearing configurations; ()* indicates mean values.~~

~~To enables direct interpretation of how each design variables (geometric parameter) responds to changes in bearing configuration, each geometric parameter is presented in an individual subplot, and colours indicate different bearing arrangements.~~

~~The figure highlights how bearing-combination choices influences shaft geometry, particularly diameter and wall thickness, reflecting different load transfer mechanisms.~~

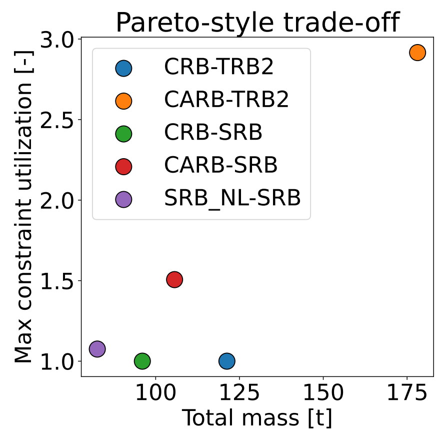

Figure 19. Pareto-style trade-off comparison of total system mass and maximum constraint for different main bearing configurations

~~Non-MR setups are seen to converge to a higher bearing span distance L_{12}. This is because they result in higher bearing forces (Eqs.1, 2, and Fig.5) which the model tries to lower by increasing the span distance, being inversely related to the bearing forces. Consequently, the LSS masses (m_{lss}) in non-MR setups are more than MR setups. On the other hand, MR-systems (TRB2-based) exhibit reduced LSS mass due to internal moment support by the MR bearing arrangement, hence relieving shaft loads, however at the cost of heavier bearings (MB2) to satisfy the fatigue-life constraints at similar bearing diameters~~ The paper focuses on a sub-assembly of the complete drivetrain (namely, the main bearing and shaft system). It must be mentioned that, when the entire drivetrain is design optimized for the given site's load conditions, and the framework is expanded through the inclusion of other drivetrain components, such as the HSS and bedplate – which supports the MBSA, GB, HSS and generator, and inclusion of corresponding constraints – such as beam stresses, bearing deflection through the bedplate support and bedplate end deflection, the design drivers change in light of the total drivetrain design, hence changing the system results. The investigation of a complete drivetrain optimization and its interaction with the turbine's support structure, in a steady-state and transient setting, are planned as future work.

5 Conclusions

In light of efficient system-level ~~multi-disciplinary optimization (MDAO)~~ design optimization of floating offshore wind turbines drivetrains, the paper highlights the lack of integration of and details in drivetrain design found in the current state-of-the-art, the significance and need for coupled, reliable and fatigue-driven drivetrain modelling, and proposes to fill this gap through efficient multi-fidelity constraint gradient-based optimization ~~, enhancing NLR's `WISDEM-WEIS` MDAO frameworks~~(GBO), enhancing SoA wind turbine MDAO framework `WISDEM-WEIS`.

As a numerical example, the drivetrain components first in line in the load path from the rotor blades, i.e. the main bearing-shaft assembly is optimized for minimum mass (or maximum power-density). The criticality of fatigue in large wind turbine drivetrains as a design driver ~~and~~ is shown, along with the importance of including FLS bearing life constraints over only-ULS static structural constraints~~are shown~~, Tab.9.

Moment-reacting MB2 is shown to showcase a few benefits such as:

1. Redistributes bearing loads, lowering MB1 and MB2 radial forces (Fig.4),
2. Ignoring MB2 moments would under-predict MB2 stiffness effects and over-predict MB1 loads,
3. Reduces peak shaft bending stresses (Tab.11),
4. Consistency between bearing physics, statics, and the structural solver,
5. Gradient sensitivities are damped as moments are redistributed via stiffness.

Moreover, DLC load spectra reduction is seen in the light of efficient gradient-based design optimization, wherein conventional non-smooth `histogram`-bin-counting (LRD) is replaced with analytically-differentiable damage equivalent loads (DEL) giving consistent results with robust convergence, Tab.12.

The proposed and enhanced setup allowed efficient exploration of various viable main-bearing configurations and the design driving differences between moment-reacting and non-moment-reacting bearing supports was shown.

The optimization demonstrates that the selected main-bearing arrangement has a significant influence on the component masses, dominant contributor to total mass, and load distribution of the main-bearing-shaft system. The constraint activity analysis further highlights the governing design mechanisms. Designs with active bearing life constraints indicate that bearing fatigue performance limits further mass reduction, whereas shaft stress and deflection constraints govern configurations where bearing loads are alleviated.

Lastly, the optimal drivetrain configuration is governed by how effectively moment and axial loads are distributed between bearings and shaft to satisfy ultimate and fatigue-critical metrics, rather than purely by component sizing.

In conclusion, the present work innovates on the current state-of-the-art in ~~MDAO~~ design analysis and optimization for wind turbine drivetrains, enhancing its detailed design ~~and combining structural dynamics~~ that combines structural analysis with critical fatigue-driven metrics, and is ~~geared for further~~ ready for integration into system-level coupled wind turbine ~~analysis and optimization~~MDAO.

5.1 Future work

This work employs the conventional de-coupled (or 2-step) global-local approach, which assumes fixed hub loads throughout. However, changes in component geometry inevitably leads to variation in component (and system) properties (i.e. mass, inertia, natural frequencies, etc.), hence changing to a respective degree the turbine's dynamic response and in turn again the hub loads. As the current work aims to enhance the drivetrain module within SoA FOWT MDAO frameworks, delineate

Table 12. Summary: GBO behaviour vs.FLS-load reduction method; *Abbreviations:* FD-finite difference, AG-analytical gradients.

Approach	Gradient Quality	GBO Behavior
LRD + FD	Noisy, discontinuous	Inconsistent convergence/failure
LRD + AG	Not possible (not differentiable)	-
Smooth DEL + FD	Sufficient	Converges reliably
Smooth DEL + AG	Exact	Faster, robust and efficient convergence

the design methodologies and results, future work is planned to push beyond the said limitations and report insights into system-level interactions, eg. between the drivetrain, the support-structure and control strategy, through fully-coupled FOWT design optimizations.

~~Future work aims to include more accurate and detailed bearing life calculations (TS 16281 ISO (2025)), analytical derivatives for bearing FLS constraints and illustrating optimization efficiency improvements due to it. Moreover, work is on-going~~ To this end, work is completed in incorporating detailed main-bearing-shaft assembly ~~and gearbox models within state-of-art~~ models within the SoA floating wind MDAO toolsets – steady-state (`WISDEM`) and transient control co-design (`WEIS`), ~~and~~ thereby enhancing design capabilities of its drivetrain module. Future work aims at reporting innovations compared to the IEA-15MW reference floating wind turbine in a system-level scope.

Future work also aims to include more accurate and detailed bearing life calculations (TS 16281 ISO (2025)), analytical derivatives for bearing FLS constraints and illustrating optimization efficiency improvements due to it.

Code availability. The methodology has been closely integrated into the open-source `WISDEM` WT-MDAO framework from NLR (2026), its drivetrain `DrivetrainSE`, the integrated wind turbine modules `WindPark`, and `.yaml` input file schemas are updated to compliment the enhancements. The code is available at the main author's `github` repository. Alongside this, the work also led to several source-code corrections in the framework's main WISDEM-GitHub (2026) repository.

Data availability. TEXT

Code and data availability. TEXT

Sample availability. TEXT

Video supplement. TEXT

Appendix A: Site-Specific Environmental Conditions

Two offshore wind site locations are considered as part of the project – Utsira-Nord, Norway and Calabira, Italy. The environmental conditions (ECs) representative of the former site (Utsira-Nord) are selected for the drivetrain design optimization as they are harsher and more severe than the latter's (Calabria), resulting in a more conservative and reliable design, applicable to both sites. For more details, the reader is referred to Made4Wind project's Deliverable 2.1 'Use case scenario' & Deliverable 5.1 Release 2.

Appendix B: Wind Turbine Specifications

The wind turbine definition, relevant for inference of this study are defined, such as turbine and drivetrain parameters Tab.B1 and materials data Tab.B2.

In Tab.B1, the drivetrain properties are kept constant throughout the design optimization process but can be included as design variables. Moreover, γ_n, the partial safety factor for the consequence of failure facilitates adjustment of the reliability level which depends on the consequence of failure (DNV-ST-0437:2024 DNV (2024), Sect.2.5.2).

In Tab.B2, σ_{yield} is the ultimate yield and $\sigma_{tensile}$ the ultimate tensile strength.

Appendix C: Stress Utilization Equations

Forces and moments in each (beam) element $(F,\ M)$ are calculated using the structural analysis tool, which are used to calculate the von-Mises stress, and further formulate the stress utilization constraint.

Herein, for a circular cross-section (eg. tube), some shorthands can be written, differentiating the axial and shear components:

- Bending modulus $S := I_y/R = I_z/R$
- Torsional shear constant $C := I_x/R$

where I is the area moment of inertia, Tab.C1.

Axial stresses:

$$M = \sqrt{M_y^2 + M_z^2}$$
$$\sigma_{axial} = \sigma_a := \frac{|F_x|}{A} + \frac{M}{S} \tag{C1}$$

Table B1. Wind Turbine Definition; (1)-defined in IEC (2019).

Property	Value [units]	Symbol	Description
Machine rating	15 [MW]	-	-
Upwind	True	-	-
Rated RPM	7.56 [rpm]	n_0	Rotor/main shaft rated rotational speed, in region-3
Rated torque	21.03 [MNm]	-	-
Lifetime	25 [years]	$L_{design,yrs}$	-
Tilt	6 [deg]	ϕ	Drivetrain main shaft tilt
Drive height	5.614 [m]	H_{drive}	Vertical distance between the hub center and tower-top center
Overhang	12.0313 [m]	$L_{overhang}$	Horizontal distance between the hub center and tower-top center
Gear-ratio	49.6 [-]	-	-
Gearbox mass	138.73 [t]	-	-
Carrier mass	27.745 [t]	$m_{carrier}$	20% of the gearbox mass
Allowable LSS deflection	10^{-4} [m]	$\delta_{defl,\ max}$	Maximum allowable deflection at the LSS-end or GB-input
Allowable LSS deflection	10^{-3} [deg]	$\delta_{ang,\ max}$	Maximum allowable angular deflection at the LSS-end or GB-input
Tower-top diameter	6.5 [m]	-	-
Partial safety factor (SF)	1.35	γ_f	Partial SF(1) for loads
Partial SF	1.3	γ_m	Partial SF for material resistance
Partial SF	1.0	γ_n	Partial SF for consequence of failure

Table B2. Steel material defined for LSS drivetrain components; The full database can be found in MatWeb.

Properties	Value
$E\ (\times 10^9)$	205
$G\ (\times 10^9)$	80
ρ	7850.0
$\sigma_{tensile}\ (\times 10^6)$	814
$\sigma_{yield}\ (\times 10^6)$	485

Shear stresses:

$$F = \sqrt{F_y^2 + F_z^2}$$

$$\sigma_{shear} = \tau := \frac{2 \cdot F}{A_s} + \frac{|M_x|}{C} \tag{C2}$$

Table C1. Area moment of inertia of a ring: cross-section of the main-shaft;
$D_o = D_{lss}$, $D_i = (D_{lss} - 2 \cdot t_{lss})$

Shape	I
Ring, through its diameter	$\cancel{I_y, I_z = \frac{\pi(D_o^4 - D_i^4)}{64}}$ $I_y, I_z = \frac{1}{64} \cdot \pi(D_o^4 - D_i^4)$
Ring, through its centre	$I_x = 2 \cdot I_y$

where, for each beam element, F_x is the axial internal force, F_y, F_z are shear forces, M_x, M_y, M_Z are moments (torque and bending), A is the cross-sectional area, and A_s is the shear area.

Thereupon, the von-Mises stress (utilization) can be calculated as (Budynas et al. (2021)):

$$\sigma_v := \sqrt{\sigma_a^2 + \sigma_h^2 - (\sigma_a \cdot \sigma_h) + 3\tau^2} \tag{C3}$$

where, σ_h is the hoop stress.

Appendix D: Tilting stiffness of moment-reacting bearings and its empirical estimation

The tilting or rotational stiffness of a moment-reacting bearing (k_θ in Nm/rad) is the amount of moment that must be applied to rotate the bearing inner ring by one radian relative to the outer ring.

Large multi-megawatt (15 MW) wind turbine's drivetrains require components such as main-bearings (3-4 m in diameter, Tab.9) that go beyond those currently available in manufacturers' catalogue. Therefore for an empirical estimation of its tilting stiffness, a database is created from known bearing specifications (Wang et al. (2020), Tab.A4), and a linear regression power-law is fitted relating the bearing bore diameter (D) to the bearing's tilting stiffness (k_θ) (similar to Sect.2.4.1); the results are shown in Fig.D1, and the empirical equation is given in Eq.D1.

$$k_\theta = 0.47083 \cdot D^{3.0580} \tag{D1}$$

where D is in [mm] and k_θ in [Nm/rad].

The coefficient of determination (R-squared score) of the estimated empirical relation is roughly 0.795.

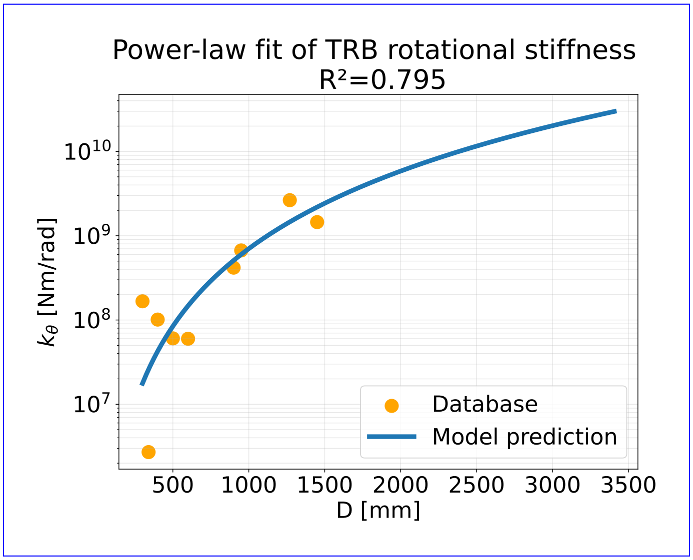

Figure D1. Empirical estimation of TRB2 tilting stiffness through linear regression power-law

Appendix E: Miscellaneous

E1 Error Functions

In the following, $\mathbf{y} = [y_i]$ and $\hat{\mathbf{y}} = [\hat{y}_i]$ are data point vectors (of equal length $= n$) corresponding to the true value and the predicted value respectively.

MAPE (Mean Absolute Percentage Error) is defined as:

$$\mathrm{MAPE} = \frac{1}{n}\sum_{i=1}^{n}\left|\left(\frac{y_i - \hat{y}_i}{y_i}\right)\cdot 100\right| \tag{E1}$$

E2 Abbreviations

A list of abbreviations used throughout the paper can be found in Tab. E1.

Author contributions. **VG**: Conceptualization, Data curation, Formal analysis, Investigation, Methodology, Project administration, Resources, Software, Validation, Visualization, Writing (original draft preparation and editing); **ARN**: Funding acquisition, Project administration, Supervision, Writing (review).

Competing interests. The co-author Amir R. Nejad is a member of the editorial board of the Wind Energy Science (WES) journal.

Disclaimer. TEXT

Acknowledgements. The authors acknowledge the financial support from the European Commission under the Horizon Europe framework programme through the Made4Wind project (no. 101136096). ~~Moreover,~~ They also thank project partner SINTEF and their researcher Serag-Eldin Abdelmoteleb for conducting high-fidelity aero-elastic turbine simulation in `SIMA` software. Lastly, the authors acknowledge the use of generative artificial intelligence (~~AI~~GenAI) and large language model (LLM) open-access tools ~~were used~~ as general assistants in tasks such as coding, understanding scientific concepts ~~,~~ and debugging.

References

ISO 281:2007: Rolling bearings — Dynamic load ratings and rating life, International Organization for Standardization, 2007.

IEC 61400-4: Design requirements for wind turbine gearboxes, 2012.

IEC 61400-1:2019: Wind energy generation systems - Part 1: Design requirements, International Electrotechnical Commission, 2019.

ISO 16281:2025: Rolling bearings — Methods for calculating the modified reference rating life for universally loaded rolling bearings, International Organization for Standardization, 2025.

Allen, C., Viscelli, A., Dagher, H., Goupee, A., Gaertner, E., Abbas, N., Hall, M., and Barter, G.: Definition of the UMaine VolturnUS-S Reference Platform Developed for the IEA Wind 15-Megawatt Offshore Reference Wind Turbine, Tech. Rep. NREL/TP–5000-76773, 1660012, MainId:9434, https://doi.org/10.2172/1660012, 2020.

Barter, G. E., Sethuraman, L., Bortolotti, P., Keller, J., and Torrey, D. A.: Beyond 15 MW: A cost of energy perspective on the next generation of drivetrain technologies for offshore wind turbines, Applied Energy, 344, 121 272, https://doi.org/https://doi.org/10.1016/j.apenergy.2023.121272, 2023.

Budynas, R. G., Nisbett, J. K., and Shigley, J. E.: Shigley's mechanical engineering design, McGraw-Hill, New York, NY, eleventh edition in si units edn., ISBN 978-0-07-717145-2, oCLC: 1226062640, 2021.

Chovan, C. and Fierro, A.: Improving Bearing Life in wind turbine main shafts and gearboxes, Timken, https://www.timken.com/resources/timken-tdi-bearings-white-paper-improving-bearing-life-in-wind-turbine-main-shafts-and-gearboxes/, 2021.

Dao, C., Kazemtabrizi, B., and Crabtree, C.: Wind turbine reliability data review and impacts on levelised cost of energy, Wind Energy, 22, 1848–1871, https://doi.org/10.1002/we.2404, _eprint: https://onlinelibrary.wiley.com/doi/pdf/10.1002/we.2404, 2019.

DNV: DNVGL-ST-0437: Loads and site conditions for wind turbines, 2016.

DNV: DNV-ST-0437: Loads and site conditions for wind turbines, 2024.

Dykes, K., Damiani, R., Roberts, O., and Lantz, E.: Analysis of Ideal Towers for Tall Wind Applications, https://doi.org/10.2514/6.2018-0999.

Gaertner, E., Rinker, J., Sethuraman, L., Zahle, F., Anderson, B., Barter, G. E., Abbas, N. J., Meng, F., Bortolotti, P., Skrzypinski, W., Scott, G. N., Feil, R., Bredmose, H., Dykes, K., Shields, M., Allen, C., and Viselli, A.: IEA Wind TCP Task 37: Definition of the IEA 15-Megawatt Offshore Reference Wind Turbine, https://doi.org/10.2172/1603478, 2020.

Guo, Y., Bergua, R., van Dam, J., Jove, J., and Campbell, J.: Improving wind turbine drivetrain designs to minimize the impacts of non-torque loads, Wind Energy, 18, 2199–2222, https://doi.org/https://doi.org/10.1002/we.1815, 2015a.

Guo, Y., Parsons, T., King, R., Veers, P., and Dykes, K.: Analytical Formulation for Sizing and Estimating the Dimensions and Weight of Wind Turbine Hub and Drivetrain Components, https://doi.org/10.2172/1215033, 2015b.

Guo, Y., Parsons, T., Dykes, K., and King, R.: A systems engineering analysis of three-point and four-point wind turbine drivetrain configurations, Wind Energy, 20, 537–550, https://doi.org/10.1002/we.2022, 2017.

Gupta, V. and Nejad, A. R.: Multi-fidelity gradient-based wind turbine main-shaft assembly optimization with analytical bearing fatigue, Journal of Physics: Conference Series, 3224, 052 023, https://doi.org/10.1088/1742-6596/3224/5/052023, 2026.

Hart, E., Clarke, B., Nicholas, G., Kazemi Amiri, A., Stirling, J., Carroll, J., Dwyer-Joyce, R., McDonald, A., and Long, H.: A review of wind turbine main bearings: design, operation, modelling, damage mechanisms and fault detection, Wind Energy Science, 5, 105–124, https://doi.org/10.5194/wes-5-105-2020, 2020.

Hart, E., Stock, A., Elderfield, G., Elliott, R., Brasseur, J., Keller, J., Guo, Y., and Song, W.: Impacts of wind field characteristics and non-steady deterministic wind events on time-varying main-bearing loads, Wind Energy Science, 7, 1209–1226, https://doi.org/10.5194/wes-7-1209-2022, 2022.

Hart, E., Raby, K., Keller, J., Sheng, S., Long, H., Carroll, J., Brasseur, J., and Tough, F.: Main Bearing Replacement and Damage - A Field Data Study on 15 Gigawatts of Wind Energy Capacity, https://doi.org/10.2172/1992019, 2023.

Helsen, J., Vanslambrouck, K., Vanhollebeke, F., and Desmet, W.: The Dynamic Behavior Induced by Different Wind Turbine Gearbox Suspension Methods Assessed by Means of the Flexible Multibody Technique, vol. Volume 4: Dynamics, Control and Uncertainty, Parts A and B of *ASME International Mechanical Engineering Congress and Exposition*, pp. 1093–1103, https://doi.org/10.1115/IMECE2012-87321, 2012.

Ishihara, T., Wang, S., and Kikuchi, Y.: Fatigue prediction of wind turbine main bearing based on field measurement and three-dimensional elastic drivetrain model, Engineering Failure Analysis, 167, 108 985, https://doi.org/10.1016/j.engfailanal.2024.108985, 2025.

Jasa, J., Bortolotti, P., Zalkind, D., and Barter, G.: Effectively using multifidelity optimization for wind turbine design, Wind Energy Science, 7, 991–1006, https://doi.org/10.5194/wes-7-991-2022, 2022.

Link, H., LaCava, W., Van Dam, J., McNiff, B., Sheng, S., Wallen, R., McDade, M., Lambert, S., Butterfield, S., and Oyague, F.: Gearbox Reliability Collaborative Project Report: Findings from Phase 1 and Phase 2 Testing, Tech. Rep. NREL/TP-5000-51885, 1018489, https://doi.org/10.2172/1018489, 2011.

Liverud Krathe, V., Jonkman, J., Gebel, J., Rivera-Arreba, I., Nejad, A., and Bachynski-Polić, E.: Investigation of Main Bearing Fatigue Estimate Sensitivity to Synthetic Turbulence Models Using a Novel Drivetrain Model Implemented in OpenFAST, Wind Energy, 28, e70 005, https://doi.org/10.1002/we.70005, 2025.

Martins, J. R. R. A. and Ning, A.: Engineering Design Optimization, Cambridge University Press, Cambridge, UK, ISBN 9781108833417, https://doi.org/10.1017/9781108980647, 2022.

MatWeb: Materlal Property Data, https://www.matweb.com/search/DataSheet.aspx?MatGUID=38108bfd64c44b4c9c6a02af78d5b6c6&ckck=1.

Musial, W., Spitsen, P., Duffy, P., Beiter, P., Marquis, M., Hammond, R., and Shields, M.: Offshore Wind Market Report: 2022 Edition, Tech. rep., National Renewable Energy Lab. (NREL), Golden, CO (United States), https://doi.org/10.2172/1883382, 2022.

Nejad, A. R.: Modelling and Analysis of Drivetrains in Offshore Wind Turbines, chap. 3, pp. 37–101, John Wiley Sons, Ltd, ISBN 9781119097808, https://doi.org/https://doi.org/10.1002/9781119097808.ch3, 2018.

Nejad, A. R., Keller, J., Guo, Y., Sheng, S., Polinder, H., Watson, S., Dong, J., Qin, Z., Ebrahimi, A., Schelenz, R., Gutiérrez Guzmán, F., Cornel, D., Golafshan, R., Jacobs, G., Blockmans, B., Bosmans, J., Pluymers, B., Carroll, J., Koukoura, S., Hart, E., McDonald, A., Natarajan, A., Torsvik, J., Moghadam, F. K., Daems, P.-J., Verstraeten, T., Peeters, C., and Helsen, J.: Wind turbine drivetrains: state-of-the-art technologies and future development trends, Wind Energy Science, 7, 387–411, https://doi.org/10.5194/wes-7-387-2022, 2022.

NLR: WISDEM, https://github.com/WISDEM/WISDEM, 2026.

Patryniak, K., Collu, M., and Coraddu, A.: Multidisciplinary design analysis and optimisation frameworks for floating offshore wind turbines: State of the art review, Ocean Engineering, 251, 111 002, https://doi.org/10.1016/j.oceaneng.2022.111002, 2022.

Perez-Moreno, S. S., Zaaijer, M. B., Bottasso, C. L., Dykes, K., Merz, K. O., Réthoré, P.-E., and Zahle, F.: Roadmap to the multidisciplinary design analysis and optimisation of wind energy systems, Journal of Physics: Conference Series, 753, 062 011, https://doi.org/10.1088/1742-6596/753/6/062011, 2016.

Sethuraman, L., Quick, J., Dykes, K., and Guo, Y.: Exploring Optimization Opportunities in Four-Point Suspension Wind Turbine Drivetrains through Integrated Design Approaches, in: 2018 Wind Energy Symposium, American Institute of Aeronautics and Astronautics, Kissimmee, Florida, ISBN 978-1-62410-522-7, https://doi.org/10.2514/6.2018-1000, 2018.

Stirling, J., Hart, E., and Kazemi Amiri, A.: Constructing fast and representative analytical models of wind turbine main bearings, Wind Energy Science, 6, 15–31, https://doi.org/10.5194/wes-6-15-2021, 2021.

Torsvik, J., Nejad, A. R., and Pedersen, E.: Main bearings in large offshore wind turbines: development trends, design and analysis requirements, Journal of Physics: Conference Series, 1037, 042 020, https://doi.org/10.1088/1742-6596/1037/4/042020, 2018.

Veers, P.: Wind Energy Modeling and Simulation - Volume 2: Turbine and System, The Institution of Engineering and Technology, https://doi.org/10.1049/PBPO125G, 2019.

Wang, S., Nejad, A. R., and Moan, T.: On design, modelling, and analysis of a 10-MW medium-speed drivetrain for offshore wind turbines, Wind Energy, 23, 1099–1117, https://doi.org/10.1002/we.2476, 2020.

Wenske, J.: Wind Turbine System Design. Volume 1, The Institution of Engineering and Technology, https://doi.org/10.1049/PBPO142F, 2022.

WISDEM-GitHub: Drivetrain code implementation: potential inconsistencies / area of development, https://github.com/NLRWindSystems/WISDEM/issues/593, 2026.

Table E1. Abbreviations used

Abbreviation	Full-form
WT	Wind turbine
FOWT	Floating offshore wind turbine
MW	Mega-watt
DT	Drivetrain
DD	Direct-drive
GD	Geared-drivetrain
GB	Gearbox
MS	Main shaft
MB	Main bearing
MBSA	Main-bearing shaft assembly
RB	Roller bearing
CARB, CRB, SRB, SRB_NL, TRB, DRTRB/TRB2	Toroidal, cylindrical, spherical, spherical non-locating, tapered, double-row tapered RB
MR	Moment-reacting
3-pt / SMB	3-point / single MB
4-pt / DMB	4-point / double MB
NTL	Non-torque loads
LSS / MSS / ISS / HSS	Low- / medium- / intermediate- / high-speed shaft
EB	Euler-Bernoulli
U-, FLS	Ultimate-, fatigue limit state
DEL	Damage-equivalent loads
LRD	Load-revolution distribution
MDAO	Multi-disciplinary design, analysis and optimization
GBO	